Monthly Notices
of the
ROYAL ASTRONOMICAL SOCIETY

MNRAS **454,** 3166–3184 (2015) doi:10.1093/mnras/stv2252

Origin of the high $v_{\rm los}$ feature in the Galactic bar

Michael Aumer★ and Ralph Schönrich

Rudolf Peierls Centre for Theoretical Physics, 1 Keble Road, Oxford OX1 3NP, UK

Accepted 2015 September 28. Received 2015 September 7; in original form 2015 June 19

ABSTRACT

We analyse a controlled *N*-body+smoothed particle hydrodynamics simulation of a growing disc galaxy within a non-growing, live dark halo. The disc is continuously fed with gas and star particles on near-circular orbits and develops a bar comparable in size to the one of the Milky Way (MW). We extract line-of-sight velocity $v_{\rm los}$ distributions from the model and compare it to data recently obtained from the Apache Point Observatory Galactic Evolution Experiment (APOGEE) survey which show distinct high-velocity features around $v_{\rm los} \sim 200\,{\rm km\,s^{-1}}$. With an APOGEE-like selection function, but without any scaling nor adjustment, we find $v_{\rm los}$ distributions very similar to those in APOGEE. The stars that make up the high $v_{\rm los}$ features at positive longitudes l are preferentially young bar stars (age $\tau \lesssim 2$–3 Gyr) which move away from us along the rear side of the bar. At negative l, we find the corresponding low $v_{\rm los}$ feature from stars moving towards us. At $l > 10$ deg, the highest $v_{\rm los}$ stars are a mixture of bar and background disc stars which complicates the interpretation of observations. The main peak in $v_{\rm los}$ is dominated by fore- and background stars. At a given time, ∼40–50 per cent of high $v_{\rm los}$ stars occupy x_1-like orbits, but a significant fraction are on more complex orbits. The observed feature is likely due to a population of dynamically cool, young stars formed from gas just outside the bar and subsequently captured by the growing bar. The high $v_{\rm los}$ features disappear at high latitudes $|b| \gtrsim 2$ deg which explains the non-detection of such features in other surveys.

Key words: methods: numerical – Galaxy: bulge – Galaxy: evolution – Galaxy: kinematics and dynamics – Galaxy: structure.

1 INTRODUCTION

The central region of our Galaxy is dominated by a bar (Binney et al. 1991; Blitz & Spergel 1991), which consists of an X-shaped box/peanut bulge at $R < 2$ kpc (Wegg & Gerhard 2013) and a vertically thin part, the *long bar*, extending to $R \sim 4$–5 kpc (Wegg, Gerhard & Portail 2015). Recently, the Apache Point Observatory Galactic Evolution Experiment (APOGEE) survey (Allende Prieto et al. 2008) has revealed that the line-of-sight velocity $v_{\rm los}$ distributions of ∼4700 K/M giant stars towards the Galactic Centre at Galactic coordinates $l = 4$–14 deg and $|b| \leq 2$ deg exhibit distinct shoulders at high velocities $v_{\rm los} \sim 200\,{\rm km\,s^{-1}}$ (Nidever et al. 2012). This result was followed up by other surveys, which yielded differing results: on the one hand, Babusiaux et al. (2014) analysed the $v_{\rm los}$ distribution of ∼400 bar red clump stars at $l = (-6)$–10 deg and $|b| \leq 1$ deg and found hints of a distinct high $v_{\rm los}$ component at $v_{\rm los} > 200\,{\rm km\,s^{-1}}$ at positive l and additionally of a distinct low $v_{\rm los}$ component at $v_{\rm los} < -200\,{\rm km\,s^{-1}}$ at negative l. On the other hand, Zoccali et al. (2014) failed to detect distinct high or low $v_{\rm los}$ components in a survey of ∼5000 red clump stars in the central Galaxy. However, they were probing different sightlines, most of them at $|b| > 2$ deg and thus further away from the plane than the other authors, or pointing more closely towards the Galactic Centre at $l = 0$.

Bars are rotating triaxial structures which are expected to be supported mostly by stars on prograde orbits parented by the x_1 family of closed long-axis orbits (Contopoulos & Papayannopoulos 1980). These orbits have proven essential in explaining the (l, v) diagram of gas towards the Galactic Centre (Binney et al. 1991) and are thus expected to be an important ingredient for explaining any observation of the kinematics of bar stars. Molloy et al. (2015) have recently shown that they could recover a distinct high $v_{\rm los}$ peak in an *N*-body simulation of a barred galaxy if they analysed only 2:1 resonant orbits elongated along the long bar axis, i.e. x_1 orbits. They did not recover the feature when taking into account all stars. Previously, Nidever et al. (2012) and Li et al. (2014) had failed to recover the observational feature in *N*-body simulations of Milky Way (MW) like galaxies. This led Li et al. (2014) to conclude that the high $v_{\rm los}$ peak is either a spurious feature due to low numbers of stars or not connected to stars on bar orbits.

Here, we analyse a controlled simulation of a growing MW-like disc galaxy with respect to $v_{\rm los}$ distributions towards the barred galactic centre. The model galaxy features a live dark halo and is

★E-mail: Michael.Aumer@physics.ox.ac.uk

continuously fed with stellar and gas particles on near circular orbits. This type of simulation was introduced by Sellwood & Carlberg (1984) for a 2D disc but has scarcely been used since (e.g. Berrier & Sellwood 2015 for a specific problem). The disc develops a bar early on and becomes comparable in structure to the MW at later stages, which allows us to create $v_{\rm los}$ distributions and compare them to the APOGEE data.

With the help of this simulation, we explore the origin of the high $v_{\rm los}$ structures and fit the detections and non-detections into a consistent picture. We find that these features are associated with a kinematically cool population of stars running alongside the bar and likely recently captured from the Galactic disc as a consequence of bar growth.

Our paper is organized as follows: Basic information about the data and simulation is found in Section 2 (survey data, selection function) and Section 3 (simulation setup). The general evolution of disc and bar in our simulation is discussed in Section 4. Detailed kinematics are analysed in Section 5 with focus on the high $v_{\rm los}$ peak. In Section 6, we apply the APOGEE selection function and directly compare the model to the data. We also explore some variation of assumed parameters, e.g. latitude b and bar angle ϕ. In Section 7, we use the successfully identified high $v_{\rm los}$ peak for a detailed study of the contributing orbits. Finally, we conclude in Section 8.

2 OBSERVATIONS AND SELECTION FUNCTION

For kinematic data from the central bar/bulge region of the MW we use data from APOGEE (Majewski et al. 2015), an infrared, high-resolution survey, which is part of the Sloan Digital Sky Survey III (SDSS; Eisenstein et al. 2011). The fibre-spectrograph allows for 300 spectra per plate covering a spectral range of 1.51-1.7 μm in the H band. As an infrared survey, APOGEE has a unique capability to obtain information from stars in the high-extinction regions within the Galactic plane and towards the central region of the MW. We use the APOGEE data publicly available via the CAS for SDSS DR10 (Ahn et al. 2014). Throughout this work, we correct all observed stellar velocities from APOGEE to the Galactic standard of rest, using $(U, V, W)_{\rm Sun} = (14.0, 250.0, 6.0)$, in concordance with Schönrich (2012) and McMillan (2011).

Another advantage of the survey is the benign selection function described in Zasowski et al. (2013). Stars in the target magnitude range with dereddened colours $J - K_s > 0.5$ mag are targeted evenly. In the case of the central Galaxy fields used within this work, stars were targeted for $6 < H < 11$. To model the selection function, we employ the population synthesis machinery from the Schönrich & Binney (2009) model. We apply a standard Salpeter IMF with an exponent of $\gamma = -2.35$, neglecting binarity of stars. The population synthesis uses a dense grid of BASTI stellar models (Pietrinferni et al. 2004, 2009, for their colour calibrations see Bedin et al. 2005). At each distance s and age τ, we count the number of stars per mass of the initial population that would end up within the colour and magnitude selection of APOGEE. The result is shown in Fig. 1 for a fixed metallicity of $Z = 0.0217$. The use of a single, slightly supersolar metallicity is a simplification, as the inner MW has a relatively wide metallicity distribution around this value (Hill et al. 2011; Bensby et al. 2013). However, all relevant metallicities show a similar preference for the detection of young stars. As the detailed age–metallicity distributions for the relevant sightlines are not well known and the detailed connection between model galaxy and MW in terms of structure and formation history is unclear, we choose to keep the model simple and use one typical metallicity. The band

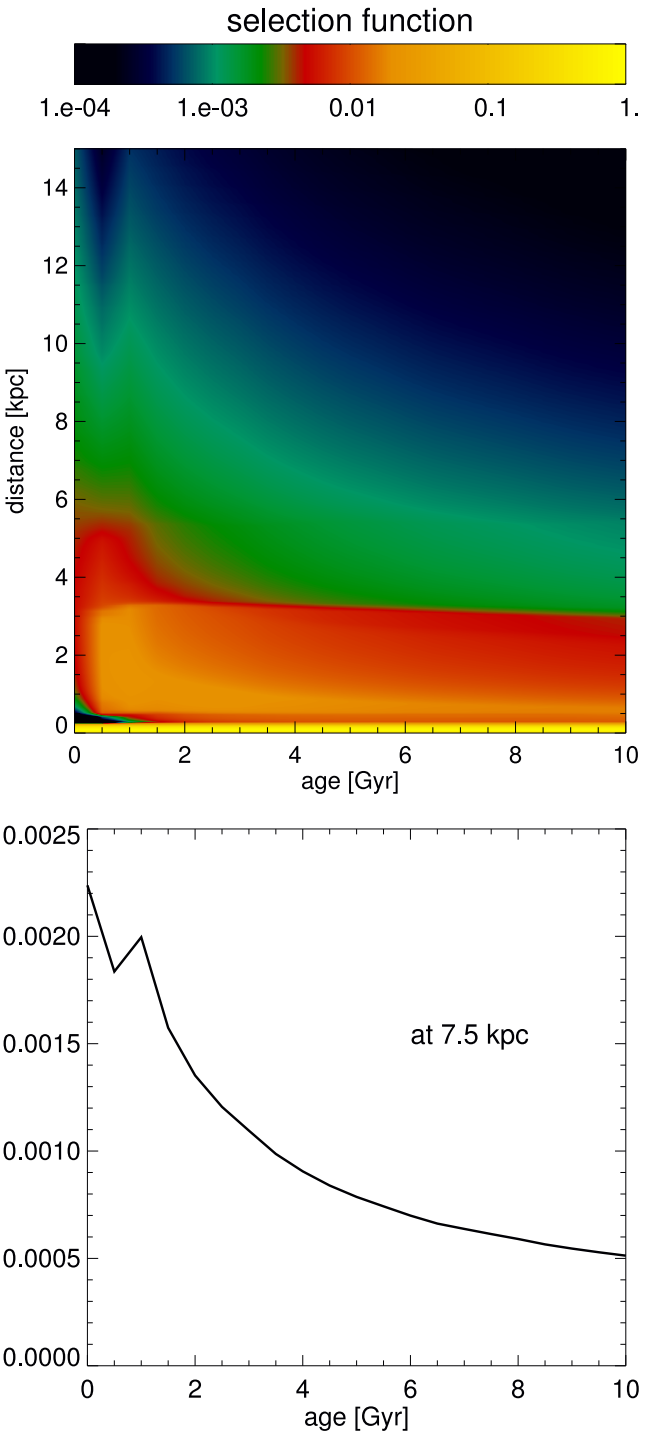

Figure 1. The selection function in distance s and age τ at a fixed metallicity of $Z = 0.0217$. Top panel: contour plot as a function of s and τ. Bottom panel: the age dependence at a typical bar distance of $s = 7.5$ kpc. Note the strong bias towards stars with ages < 2 Gyr at larger distances.

of high selection probabilities at very small distances derives from main-sequence dwarf stars. The stellar models are not fully reliable in this region for such cool dwarfs. However, this foreground is strongly suppressed by the geometric factor (s^2) of the pencil beam survey. The number of stars currently in the giant stages of interest to us declines strongly (by roughly one order of magnitude) with age, implying a strong bias in favour of young stars within the APOGEE

survey. We apply this selection function to our N-body simulation by weighting each particle with its respective selection probability. APOGEE uses dereddened magnitudes for targeting, however there are residual effects from reddening uncertainties, which we neglect here.

3 SIMULATIONS

In this paper, we present a controlled collisionless+hydrodynamic simulation of a growing galactic disc embedded in a non-growing dark matter halo. The simulations were all carried out with the Tree Smoothed Particle Hydrodynamics (TreeSPH) code GADGET-3, last described in Springel (2005). The applied gravitational softening lengths are $\epsilon_{\rm disc} = 30\,{\rm pc}$ for stellar and gaseous disc particles and $\epsilon_{\rm DM} = 100\,{\rm pc}$ for halo particles. We use an opening angle for the tree code of $\theta = 0.5$. An adaptive time-stepping scheme which assigns time steps in bins j according to $\Delta t_i = \tau/2^j < \sqrt{2\eta\epsilon_i/|\boldsymbol{a}_i|}$ to individual particles is applied. Here, $\eta = 0.02$ is an accuracy parameter and $\boldsymbol{a}_i$ is the gravitational acceleration at the position of particle i with softening ϵ_i. The base timestep τ is appropriately chosen by the code and a maximum of 10 Myr is allowed for timesteps. The hydrodynamical timestep is based on a Courant-like condition $\Delta t_{i,\,\rm hyd} \propto \kappa h_i/c_{\rm s}$, where $\kappa = 0.15$ is the Courant parameter, h_i is the smoothing length and $c_{\rm s}$ is the sound speed. We apply an isothermal equation of state $P = \rho c_{\rm s}^2$ with $c_{\rm s} = 20\,{\rm km\,s^{-1}}$ and use $N_{\rm SPH} = 48$ neighbours for the smoothing kernel. For further code details we refer to Springel (2005).

3.1 Initial conditions

To generate initial conditions (ICs) for our numerical experiments, we use the publicly available GALIC code (Yurin & Springel 2014), which produces near-equilibrium ICs of multicomponent collisionless systems with given density distributions using an iterative approach.

The initial system consists of a dark halo with a mass of $M_{\rm DM} = 0.995 \times 10^{12}\,{\rm M}_\odot$ represented by $N_{\rm DM} = 1 \times 10^6$ particles and an embedded thin galactic disc with a mass of $M_{\rm disc,\,i} = 0.5 \times 10^{10}\,{\rm M}_\odot$ represented by $N_{\rm disc,\,i} = 5 \times 10^5$ particles, so that the disc particle mass is $m_{\rm disc} = 1 \times 10^4\,{\rm M}_\odot$.

The dark halo has a Hernquist profile with

$$\rho_{\rm DM}(r) = \frac{M_{\rm DM}}{2\pi}\frac{a}{r\,(r+a)^3}. \tag{1}$$

The inner profile is adjusted so that it is similar to an NFW profile with concentration $c = 9$ and virial radius $R_{200} = 162.6\,{\rm kpc}$. This leads to a scale radius $a = 30.25\,{\rm kpc}$. The halo initially has a spherical density profile and radially isotropic kinematics, i.e. equal velocity dispersion in the principal directions, $\sigma_r = \sigma_\phi = \sigma_\theta$ and consequently a value of the anisotropy parameter of $\beta = 1 - \left(\sigma_\theta^2 + \sigma_\phi^2\right)/\left(2\sigma_r^2\right) = 0$.

The disc is set up with a mass profile

$$\rho_{\rm disc,i}(R,z) = \frac{M_{\rm disc,i}}{4\pi h_z {h_R}^2}\,{\rm sech}^2\left(\frac{z}{h_z}\right)\exp\left(\frac{-R}{h_R}\right), \tag{2}$$

with an exponential scalelength of $h_R = 1.5$ kpc and an isothermal vertical profile with a radially constant scaleheight of $h_z = 107$ pc. The vertical velocity dispersion σ_z thus declines with radius. We assume $(\sigma_z/\sigma_R)^2 = 0.5$, so that Toomre's Q shows a minimum value of $Q_{\rm min} = 1.15$ at $R \sim h_R$.

For further information regarding the ICs, we refer to Aumer et al. (in preparation). We note that here the halo is rather poorly resolved with $N_{\rm DM} = 1 \times 10^6$ and a rather short softening length ($\epsilon_{\rm halo} = 100\,{\rm pc}$) is applied. The low $N_{\rm DM}$ is due to limited computational resources and a preference to use them to resolve the disc. As expected (e.g. Dubinski, Berentzen & Shlosman 2009), purely collisionless (no SPH) tests with a higher $N_{\rm DM} = 5 \times 10^6$ show reduced disc heating and less bar slowdown. Yet the disc heating for the simulation studied here is comparable to the MW, with similar velocity dispersions for 10 Gyr old solar neighbourhood stars, since heating by massive halo particles compensates the lack of heating by giant molecular clouds or other sources such as satellite galaxies. As far as bar slowdown due to angular momentum transfer to the halo is concerned, the radius and rotation frequency of bars differ by less than ~ 20 per cent at late times (6–10 Gyr), the time relevant for this work.

3.2 Feeding the disc

To model the continuous growth of galactic discs via star formation and gas accretion we, over a timespan of 10 Gyr, add new particles with $m_{\rm disc} = 1 \times 10^4\,{\rm M}_\odot$ to the existing disc every 5 Myr. We assume a mass growth rate history given by

$$\dot{\rm M}(t) = \dot{\rm M}_0 \times \exp\left(-\frac{t}{t_{\rm feed}}\right), \tag{3}$$

with an exponential decay time-scale $t_{\rm feed} = 8\,{\rm Gyr}$, which is motivated by the findings of Aumer & Binney (2009), and a normalization $\dot{\rm M}_0 = 8\,{\rm M}_\odot\,{\rm yr}^{-1}$, so that a total of $\sim 4.5 \times 10^{10}\,{\rm M}_\odot$ are fed over 10 Gyr. The added disc mass is radially distributed as $\rho(R) \propto \exp\left(-R/h_R(t)\right)$, with an exponential scalelength that increases with time as

$$h_R(t) = \left(1.5 + \frac{\left(h_{R,\rm final} - 1.5\right)}{\sqrt{10}}\sqrt{\frac{t}{1\,{\rm Gyr}}}\right)\,{\rm kpc}. \tag{4}$$

This increase from $h_R = 1.5\,{\rm kpc}$ to a scalelength at 10 Gyr $h_{R,\,\rm final} = 4.3\,{\rm kpc}$ is motivated by the findings of Bovy et al. (2012). The particles are randomly scattered over azimuth ϕ and placed at $z = 0$. The coordinate system is regularly updated to be centred on the centre of mass of the system.

The particles are assigned near circular orbits. We determine the new particles' rotational velocities as $v_{\phi,i} = \sqrt{a_{R,i}\,R_i}$ for a particle i at cylindrical radius R_i and the component of the gravitational acceleration pointing towards the centre, $a_{R,\,i}$. For stellar particles, we add random velocity components in all three directions ϕ, R and z, drawn from Gaussian distributions with $\sigma = 6\,{\rm km\,s^{-1}}$.

After a disc goes bar unstable, there are no stable circular orbits in the bar region. So we impose an inner cutoff radius $R_{\rm cut}$, within which no particles are introduced. We use the radius where the logarithm of the $m = 2$ Fourier amplitude $\ln(A_2)$ drops below -1.5 as an inner cutoff radius.

3.3 The gas component

In disc galaxies, bars slow down and grow in size due to the transfer of angular momentum to the dark halo (Debattista & Sellwood 2000). This loss is to some extent balanced by the transfer of angular momentum from the gas to the bar (Berentzen et al. 2007). Therefore, it is desirable to include a gas component in barred disc galaxy models. We do not wish to introduce a full model containing the accretion of gas on to the galaxy, its cooling and the subsequent star formation and feedback processes (see e.g. Roškar et al. 2012 for an isolated galaxy model), as uncertainties regarding the modelling of

the physical processes are high (see e.g. Fraternali & Binney 2008; Nelson et al. 2013).

To keep the model simple, we add a constant fraction of gas to our galactic disc and model it with an isothermal equation of state $P = \rho c_s^2$ with $c_s = 20\,\mathrm{km\,s^{-1}}$. We simulate the growth of the disc by continuously adding stellar and gas particles. The initial gas disc is created by turning 5 per cent randomly chosen stellar particles into SPH particles. This mild disturbance of the ICs is unimportant compared to the rapid onset of disc instability in the growing galaxy. During disc growth we aim at a gas mass fraction in the disc of 10 per cent as observed in modern day MW like disc galaxies. We achieve this by adding 10 per cent of new particles as gas when the mass fraction of gas in the galaxy is above 10 per cent, and by adding 20 per cent of new particles as gas when the mass fraction of gas is lower.

Computationally, high gas densities in the central galaxy are very expensive. Therefore, we include a number of measures to limit the central density. (i) Prior to the bar forming and the inner cutoff on particle insertion coming into play, we create no gas particles at $R < 1\,\mathrm{kpc}$. (ii) We include a model for star formation in the very central galaxy. We turn SPH particles with hydrogen number densities $n > n_{\rm th} = 10\,\mathrm{cm^{-3}}$ and specific angular momentum $j < j_{\rm th} = 100\,\mathrm{km\,s^{-1}\,kpc}$ into star particles with a probability $p = \eta t_{\rm dyn}/\Delta t_i$, where $\eta = 0.1$ is an efficiency parameter, $t_{\rm dyn} = 1/\sqrt{4\pi G\rho}$ is the local dynamical time-scale and Δt_i is the timestep of the particle. To mimic the effect of a central galactic outflow (Bland-Hawthorn & Cohen 2003), we only turn one out of five particles into a star and remove the other four out of five from the simulation. Note that only gas particles in the inner bar region are affected by these prescriptions.

4 STRUCTURE OF THE BARRED DISC

In this section, we discuss the structure of our model of a barred disc galaxy. Note that we are comparing a specific – and in no way fitted – model to a specific galaxy, the MW. Though our model should not provide a perfect match to our Galaxy, we expect the model to qualitatively share important characteristics. Note that due to computational limitations, we currently have only one model of this type including hydrodynamics available.

In Fig. 2, we present the evolution of bar parameters in our simulation. We determine a bar radial extent $R_{\rm bar}$ by first calculating the $m = 2$ Fourier amplitude profile

$$A_2(R) = \frac{1}{N(R)} \sum_{j=1}^{N(R)} e^{2i\phi_j}, \tag{5}$$

where $N(R)$ is the number of particles in the radial bin centred on R and we only take into account stellar particles. Then we define $R_{\rm bar}$ as the radius where $\ln A_2(R)$ drops below -1.5 or as zero if it never reaches the value in the central area.

In the left-hand panel of Fig. 2, we see that the bar forms in the first Gyr, but its radius and strength are varying significantly. From $t \sim 1$ Gyr on the bar grows almost linearly in time to reach $R_{\rm bar} \sim 4\,\mathrm{kpc}$ at $t \sim 9$ Gyr. Our definition for $R_{\rm bar}$ allows no exact comparison to the values cited for the length of the MW long bar. Wegg et al. (2015) determine a length of 5 kpc and give 4 kpc as a lower limit, not in disagreement with our model.

In the middle panel of Fig. 2, we present the evolution of the bar rotational frequency $\Omega_{\rm bar}$ determined by following the angle of the bar major axis from snapshot to snapshot. The bar initially rotates with a frequency of 60–80 $\mathrm{km\,s^{-1}\,kpc^{-1}}$, but as the loss of angular momentum to the halo is not balanced by the transfer of angular momentum from the inflowing gas component, $\Omega_{\rm bar}$ steadily declines to reach $\sim$25 $\mathrm{km\,s^{-1}\,kpc^{-1}}$ at the end of the simulation. For the MW bar this quantity is little constrained. While our value is lower than most estimates for the MW (Dehnen 2000; Antoja et al. 2014; Sormani, Binney & Magorrian 2015), the value is in concordance with a recent estimate by Portail et al. (2015a, see their section 8.3 for a discussion of deduced MW bar pattern speeds). Our model is thus at the lower end of values inferred for the MW.

In Fig. 3, we present surface density projections of the whole galaxy model and the bar region at a simulation time $t = 7.3$ Gyr. The lower panels show face-on views of the stellar and the gaseous components. Apparently, the galaxy is dominated by the bar within $R = 4\,\mathrm{kpc}$ and shows flocculent spiral structure at outer radii. The upper panels give close ups of the bar region. The face-on view shows two distinct radial regions in terms of minor axis extent. At $R < 2\,\mathrm{kpc}$, the bar shows a mildly elongated structure, at $R = 2$–$4\,\mathrm{kpc}$ a thinner, long bar structure is visible. The edge-on

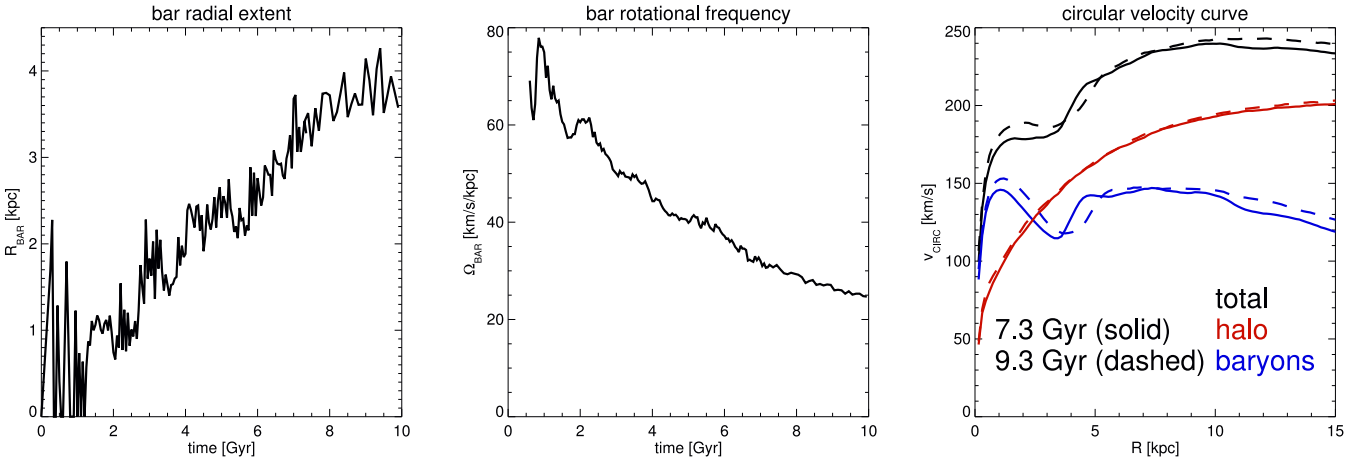

Figure 2. The evolution of bar parameters with time: Left: the bar radial extent $R_{\rm bar}$, defined as the radius where the logarithm of the $m = 2$ Fourier amplitude $\ln(A_2)$ drops below -1.5. Middle: the rotational frequency of the bar $\Omega_{\rm bar}$. Right: the azimuthally averaged circular velocity curve $v_{\rm circ}(R)$ in the plane of the model galaxy at 7.3 Gyr (solid) and 9.3 Gyr (dashed). The contributions from the dark halo are shown in red and the contributions from the baryons are shown in blue.

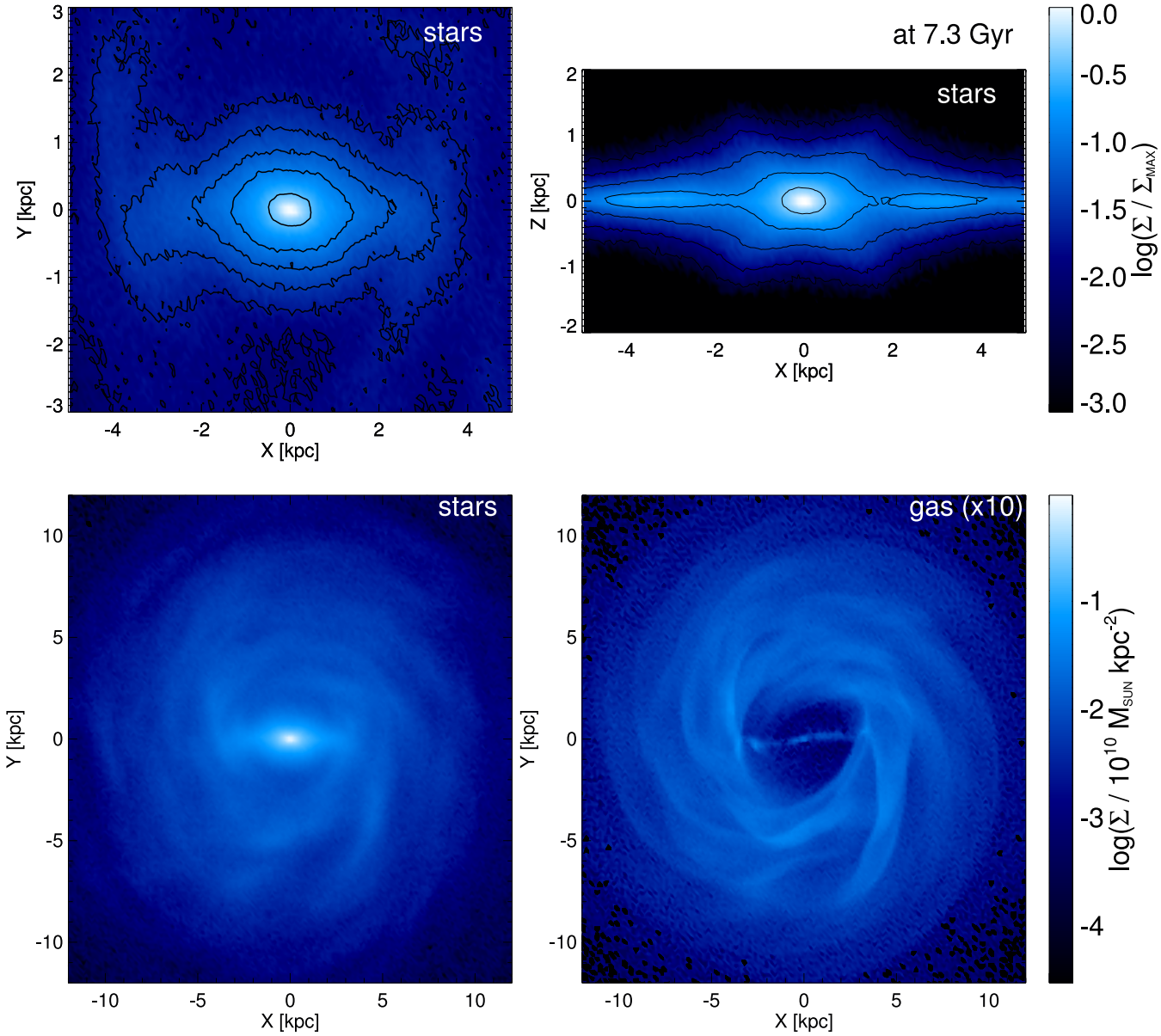

Figure 3. Stellar surface density Σ projections of our galaxy model at 7.3 Gyr. Top left: a face-on view of the bar region. Top right: an edge-on view of the bar region. Only stars within 2 kpc of the $x - z$ plane are considered. Bottom left: a face-on view of the stellar disc. Bottom right: a face-on view of the gas disc. The gas surface density was enhanced by a factor of 10.

view reveals, that the region $R < 2$ kpc is dominated by an X-shaped structure with the tips of this structure at $(x, z) \sim (2, 1.3)$ kpc, very similar to the structure of the MW bulge/bar region inferred by Wegg & Gerhard (2013). This view also shows that the outer bar is significantly thinner. Around the tips of the bar we measure a vertical exponential scaleheight of 180 pc, similar to the long bar scaleheight inferred by Wegg et al. (2015), but without a superthin 45 pc component as found by these authors. Such a component is likely too thin to be resolved in our simulation, considering our softening length of 30 pc.

At a solar neighbourhood like radius $R = 8$ kpc, we find that our model at 7.3 Gyr has a stellar exponential scalelength of 3.5 kpc, which grows mildly towards 10 Gyr. The disc is thus likely more extended than that of the MW, for which estimates usually range at 2–3 kpc. The model has a total baryonic mass of $4.2 \times 10^{10}\,\mathrm{M}_\odot$ at 7.3 Gyr, it has grown from a mass of $0.5 \times 10^{10}\,\mathrm{M}_\odot$ at $t = 0$.

In the right-hand panel of Fig. 2, we plot the circular velocity curve $v_{\rm circ}(R)$ in the plane of the model galaxy at 7.3 and 9.3 Gyr. The contributions from dark matter and baryons are shown in red and blue. We measure $v_{\rm circ} = \sqrt{a_R R}$ by calculating the component of the gravitational acceleration pointing towards the centre a_R on an (R, ϕ) grid at $z = 0$ and at each R average over the equally distributed values of ϕ. We note that the circular velocity curve in the centre of the MW is not well constrained and that it is uncertain how the observations of gas velocities in the MW bar are connected to our definition of $v_{\rm circ}(R)$. There is only mild evolution from 7.3 to 9.3 Gyr visible in $v_{\rm circ}(R)$.

The circular velocity curves show features at the bar radius, deriving from the baryonic matter distribution. The reason for these features is that the bar redistributes matter towards the centre, whereas by construction of the model new baryons are added outside the bar region, which gives rise to the baryonic dip at $R \sim 3$ kpc. In our

model, the baryonic contribution to the circular velocity is greater than the dark matter equivalent only within $R \sim 2.5$ kpc. It is unclear how this relates to the MW, but our model agrees with two important constraints. (i) At $R = 8$ kpc and 7.3 Gyr we recover $v_{\rm circ} = 236\,{\rm km\,s^{-1}}$, in good agreement with what Schönrich (2012) finds from local kinematics. (ii) The total dark matter mass within a sphere of $r = 8$ kpc is $6.3 \times 10^{10}\,{\rm M}_{\odot}$ in good agreement with the dark matter mass within a sphere of solar Galactic radius that Piffl et al. (2014) have deduced.

At the evolution stages relevant for this paper, the model has a slow bar with $R_{\rm bar} \sim 0.5 R_{\rm CR}$, where $R_{\rm CR}$ is the bar corotation radius. This is likely connected to the fact that our galaxy model is *sub-maximum*, i.e. the dark matter contribution to the circular velocity curve is significant in the bar/disc region, as fast bars with $R_{\rm bar} = 0.7$–$1.0 R_{\rm CR}$ are thought to require *maximum* discs with baryon-dominated circular velocity curves (Debattista & Sellwood 2000).

5 $v_{\rm los}$ DISTRIBUTIONS

In the previous section, we have shown that the bar emerging in our galaxy model has comparable structural parameters to the MW bar. We now extract line-of-sight velocity $v_{\rm los}$ distributions from our model and qualitatively compare them to the results of Nidever et al. (2012). In this section, we limit ourselves to the general understanding of the observed phenomena. We will attempt a quantitative comparison to observed data in the following section.

5.1 $v_{\rm los}$ distributions for the bar region

As we expect stars moving along the major axis of the bar to be the source of the stars that comprise the high $v_{\rm los}$ peak, we focus here on the central region of the model, defined by galactocentric $R < 4$ kpc. The full model including the selection function will be discussed in the next section.

To create $v_{\rm los}$ distributions, we place ourselves at a solar radius of $R = 8.3$ kpc (McMillan 2011) and orient the bar to an angle of ϕ between its major axis and the Sun–Galactic Centre sightline. Values found for ϕ in the literature range between 15 and 40 deg. For most of this paper, we choose $\phi = 20$ deg and show in the next section that our conclusions are unchanged for the full range of cited values. We usually define sightlines which are 2 deg wide in l and b and centred on the given values. To curb Poisson noise, we use the π ($m = 2$) symmetry of the model and use two sightlines per snapshots, 180 deg apart in azimuth. For each plot we stack 50 snapshots, separated in time by 1 Myr and rotate the bar to achieve the same value of ϕ for each snapshot.

In Fig. 4, we show $v_{\rm los}$ histograms at latitudes $|b| < 1$ deg at a simulation time of 7.3 Gyr for eight different longitudes l between 14 and -10 deg. The figure shows histograms for all bar stars with $R < 4$ kpc in blue and for the subset of young star particles with ages <2 Gyr in red. The $v_{\rm los}$ distributions for all stars (blue lines) do not reveal significant features at high velocities. This is consistent with recent examinations of simulations in Nidever et al. (2012), Li et al. (2014) and Molloy et al. (2015), who also detected no features when all stars are taken into account.

Nidever et al. (2012) reported peaks of high-velocity stars with $v_{\rm los} \sim 200$–$250\,{\rm km\,s^{-1}}$ of varying extent for longitudes l between 14 and 4 deg and Babusiaux et al. (2014) reported such peaks for $l = 10$ and 6 deg and a peak at $v_{\rm los} \sim -225\,{\rm km\,s^{-1}}$ at $l = -6$ deg. Closer inspection of the blue histograms at $l = \pm 6$ and ± 10 deg reveals an excess of stars at the expected $v_{\rm los}$ values. Moreover, the position of the main peak in the $v_{\rm los}$ distribution decreases with decreasing l as observed by Nidever et al. (2012). These main peaks of the distributions are, however, wider in the model than in the observation.

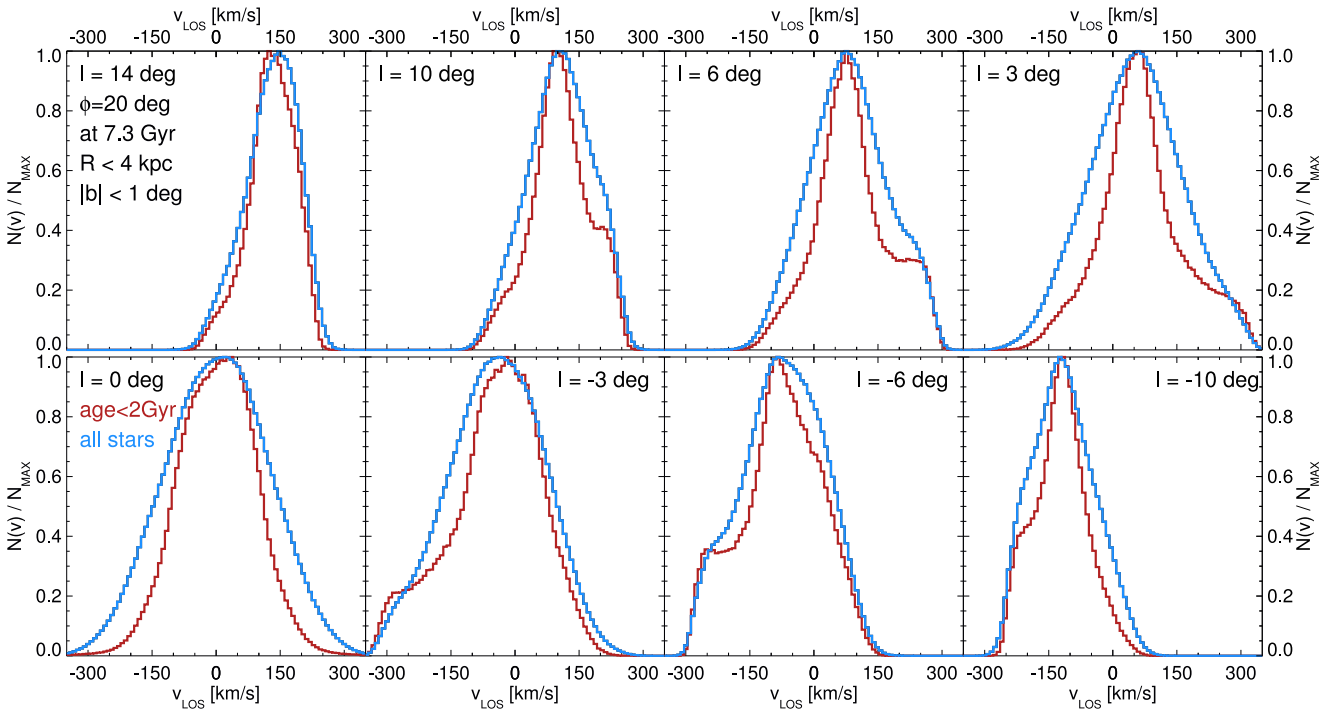

Figure 4. Line-of-sight velocity $v_{\rm los}$ distributions $N(v_{\rm los})/N_{\rm max}$ of stars at $R < 4$ kpc as seen from $R = 8.3$ kpc at a bar angle of $\phi = 20$ deg for eight different viewing longitudes $l = 14$–(-10) deg. We consider stars at latitudes $|b| < 1$ deg and all panels cover 2 deg width in l. We show the distributions for all stars (blue) and stars younger than 2 Gyr (red). The $v_{\rm los}$ bins used here are all $8\,{\rm km\,s^{-1}}$ wide.

The fact that the APOGEE selection function (Fig. 1) favours young stars motivates to examine only stars with ages <2 Gyr shown as red curves. Note that stars formed from low angular momentum central gas do not play a role for this analysis and are excluded here. The main $v_{\rm los}$ peaks are much narrower for young stars than for all stars, indicating that these populations are cooler. The red histograms clearly show distinct components at $v_{\rm los} = 200$–$300\,{\rm km\,s^{-1}}$ for $l = 3, 6$ and 10 deg and at $v_{\rm los} = -300$–$(-200)\,{\rm km\,s^{-1}}$ for $l = -3$, -6 and -10 deg, in agreement with observations. Interestingly, we do not recover a separate component at $l = 14$ deg, where Nidever et al. (2012) also claimed to find a distinct high $v_{\rm los}$ peak, a finding which we will return to in the next section.

5.2 Evolution with time and age

As the model young populations show the observed signature, it is interesting to ask whether this is specific to a unique time or stage of bar evolution or a generic feature of young stars. In Fig. 5, we examine the evolution of young stellar populations with time plotting the populations which at respective times are less than 2 Gyr old. We consider simulation times 7.3, 8.3 and 9.3 Gyr. We notice several points. (i) There is very little change in the general shape of the histograms and in the position and width of the main $v_{\rm los}$ peaks at all longitudes l. (ii) The extreme values of $v_{\rm los}$ increase with time by around $20\,{\rm km\,s^{-1}}$ for all sightlines which do not cross the galactic centre. (iii) The high $|v_{\rm los}|$ peaks identified in Fig. 4 become slightly more distinct in time and also move to higher velocities. (iv) For 9.3 Gyr additional features/peaks become apparent at the opposite side of the main peaks, e.g. at $-150 < v_{\rm los}/\,{\rm km\,s^{-1}} < -50$ at $l = 6$ deg or at $0 < v_{\rm los}/\,{\rm km\,s^{-1}} < 100$ at $l = -6$ deg.

The high $v_{\rm los}$ features at positive longitudes and low $v_{\rm los}$ features at negative longitudes are thus stable over time and not connected to any temporary phenomenon. Due to the lack of opposite peaks in the APOGEE data, we will focus our analysis on the simulation time 7.3 Gyr.

So far we have shown that young stars show high $|v_{\rm los}|$ peaks, whereas the whole population of bar stars does not. It is thus interesting to study in more detail how the $v_{\rm los}$ distribution evolves with age. We attempt this in Fig. 6, where we concentrate on one sightline, $l = 6 \pm 1$ degrees, for which both our simulation and APOGEE data display a peak at high $v_{\rm los}$.

Panel E shows how the $v_{\rm los}$ distribution varies when stars are sorted in four different age bins. Whereas the high $v_{\rm los}$ population is very distinct for stars with ages below 1 Gyr, this population becomes less distinct at higher ages. For stars with ages between 1 and 2 Gyr, it is still clearly visible, at 2–4 Gyr only a small feature remains and for older stars even this weak signature vanishes. The vanishing of the distinct high $v_{\rm los}$ population goes hand in hand with broadening of the main $v_{\rm los}$ peak indicating a heating of the population.

To see how this evolves with simulation time, we plot in panels A–D stars in these age bins at three different simulation times, 7.3, 8.3 and 9.3 Gyr. We notice that there is much less evolution with simulation time than there is with age. The level of distinction of the high $v_{\rm los}$ signature remains similar at all considered simulation times for each age bin.

To strengthen these findings, we plot in panel F of Fig. 6 the population of stars born between 6.3 and 7.3 Gyr at three different times representing mean population ages 0.5, 1.5 and 2.5 Gyr. This underlines that the evolution of the $v_{\rm los}$ distribution with age shows the broadening of the main $v_{\rm los}$ peak due to heating and the gradual loss of the high $v_{\rm los}$ peak.

We again notice that the young populations of stars at 9.3 Gyr show additional features at the opposite side of the main peak.

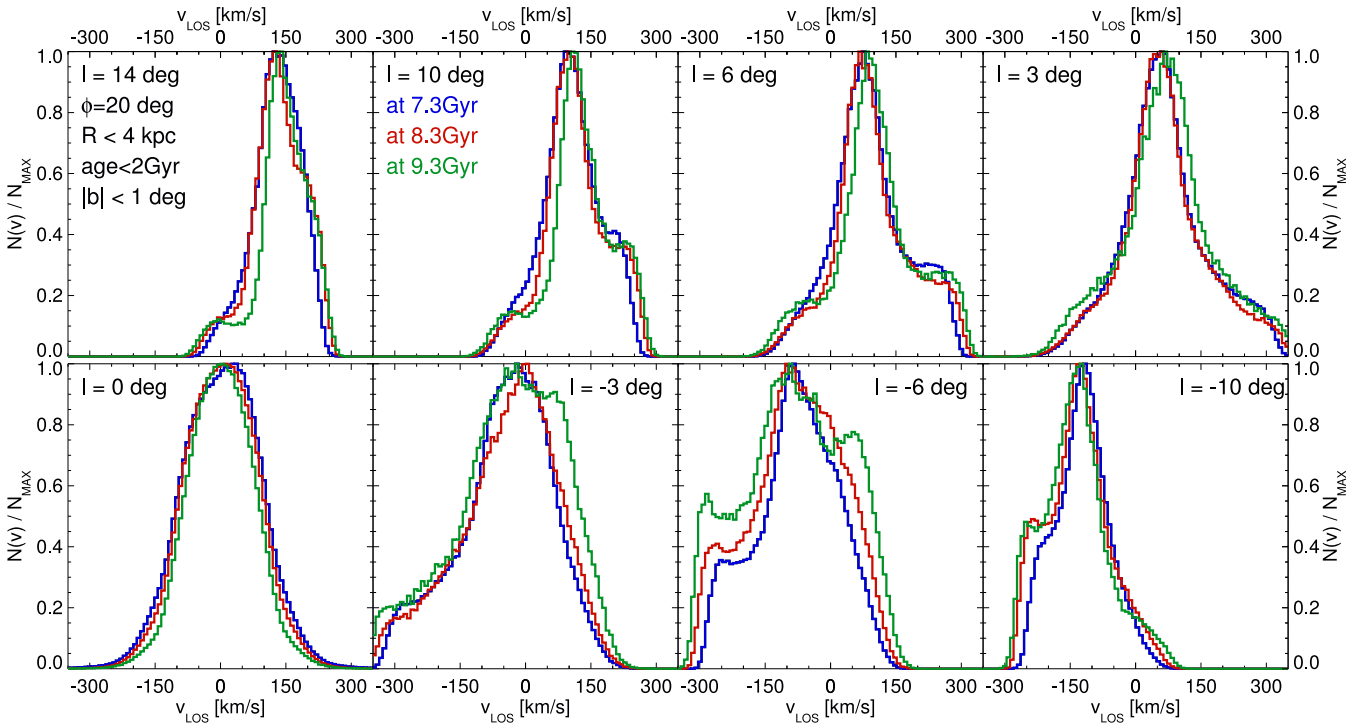

Figure 5. Line-of-sight velocity $v_{\rm los}$ distributions $N(v_{\rm los})/N_{\rm max}$ of young stars with ages <2 Gyr at $R < 4\,{\rm kpc}$ as seen from $R = 8.3\,{\rm kpc}$ at a bar angle of $\phi = 20$ deg for eight different viewing longitudes $l = 14$–(-10) deg. We consider stars at latitudes $|b| < 1$ deg and all panels cover 2 deg width in l. We show the distributions for stars at three different times: 7.3 (blue), 8.3 (red) and 9.3 Gyr (green). The $v_{\rm los}$ bins used here are all $8\,{\rm km\,s^{-1}}$ wide.

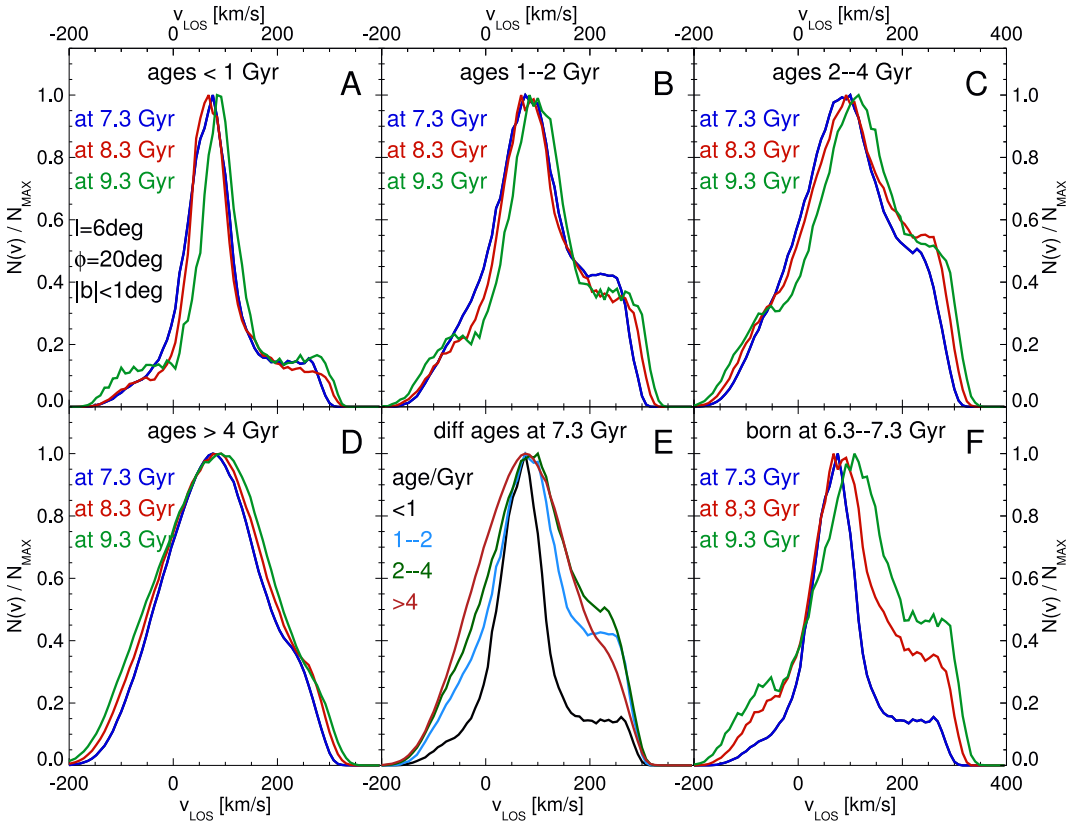

Figure 6. Line-of-sight velocity v_{los} distributions $N(v_{los})/N_{max}$ of stars at $R < 4$ kpc as seen from $R = 8.3$ kpc at a bar angle of $\phi = 20$ deg at longitudes $l = 6 \pm 1$ deg and latitudes $|b| < 1$ deg. v_{los} bins used here are all 8 km s^{-1} wide. Panels A–D: populations of stars at four fixed age bins, <1 Gyr, 1–2 Gyr, 2–4 Gyr and >4 Gyr at three different simulation times: 7.3 (blue), 8.3 (red) and 9.3 Gyr (green). Panel E: populations of stars at the four age bins <1 Gyr (black), 1–2 Gyr (blue), 2–4 Gyr (green) and >4 Gyr (red) at simulation time 7.3 Gyr. Panel F: the population of stars born between 6.3 and 7.3 Gyr in the simulation as viewed at 7.3 (blue), 8.3 (red) and 9.3 Gyr (green).

Closer inspection reveals hints of this feature also at earlier times. Additionally, the main peaks move to higher v_{los}. We will provide an explanation for these changes in Section 7. We note, however, that these additional peaks are only visible if we select young bar stars. When applying the selection function on all stars along the line of sight, as described in the next section, these features, unlike the conventional high v_{los} peaks, are too small to be detected.

6 COMPARISON TO APOGEE DATA

In the previous section, we have shown that populations of young bar stars are expected to display high $|v_{los}|$ features as observed by Nidever et al. (2012) and Babusiaux et al. (2014). In reality, not only stars with $R < 4$ kpc will contribute to the APOGEE v_{los} distributions, but also disc stars in front of or behind the bar. In the following, we directly compare the *N*-body simulation to the APOGEE data, applying the selection function described in Section 2.

6.1 The effect of the selection function

We start with Fig. 7, where we compare the v_{los} histograms for stars with galactocentric radii $R < 4$ kpc (see previous section) to v_{los} histograms obtained for the full sightlines. We do so for three longitudes, $l = \pm 6$ and 14 deg. The blue curves represent all stars within 4 kpc and the red curves show the subset of young stars, both are taken from Fig. 5. The velocity distributions for all stars along the sightline (equally weighted, green) are strikingly different. Their main v_{los} peaks are significantly narrower and shifted by more than 50 km s^{-1} towards zero. This is due to the dominant contribution by fore- and background disc stars, which are kinematically cold and are observed with the local azimuthal direction nearly perpendicular to the line of sight.

We noticed above that no distinct high $|v_{los}|$ feature is found for all stars at $R < 4$ kpc. Interestingly this is not true for all stars along the line of sight. In this population, the feature is less distinct than the one for young bar stars, but lies at the same v_{los} range. The histograms obtained when weighting all stars along the line of sight according to the selection function presented in Section 2 are shown as black lines. Overall, they resemble more the ones for all stars along the line of sight than to the ones for stars at $R < 4$ kpc. When present, the high $|v_{los}|$ feature is strengthened by the selection function and the main peak is shifted to slightly larger $|v_{los}|$.

From these comparisons, we conclude that the v_{los} distribution is not only shaped by stars in the bar region, but by all stars along the line of sight. This is illustrated by the selection function weighted (SFW) distribution of stars along the line of sight $c(s)$ as a function of distance from the Sun s in the left-hand panels of Fig. 8 (dashed lines). Clearly, the SFW distribution functions do not simply reflect the density distributions along the pencil beams, but are shaped by the age- and distance-dependent selection function modulated by the beam area increasing as s^2. Of the three shown sightlines, only the one which crosses the bar most centrally ($l = 6$ deg) has its absolute maximum coincident with the bar distance. The loci of young stars, the highest densities of which are by construction

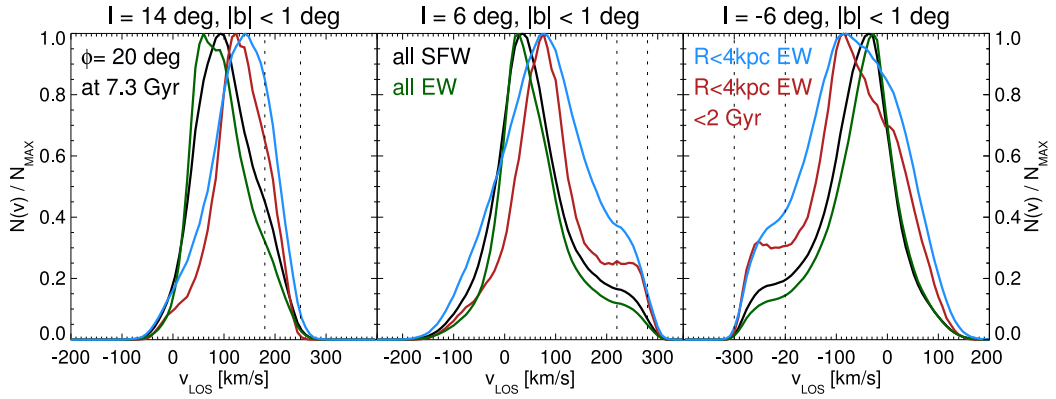

Figure 7. Line-of-sight velocity $v_{\rm los}$ distributions $N(v_{\rm los})/N_{\rm max}$ of stars at longitudes $l = 14 \pm 1$, $l = 6 \pm 1$ and $l = -6 \pm 1$ deg and latitudes $|b| < 1$ deg. We assume a bar angle of $\phi = 20$ deg, a solar radius of $R = 8.3$ kpc and use $v_{\rm los}$ bins which are all 8 km s^{-1} wide. We compare four different types of histograms: blue considering all stars at $R < 4$ kpc, equally weighted (EW), red considering young stars with ages <2 Gyr at $R < 4$ kpc, equally weighted, green considering all stars along the sightline, equally weighted and black considering all stars along the sightline, weighted according to the age- and distance-dependent selection function SF(s, τ) from Fig. 1 (SFW). The vertical dashed lines indicate the intervals for peak stars considered for Fig. 8.

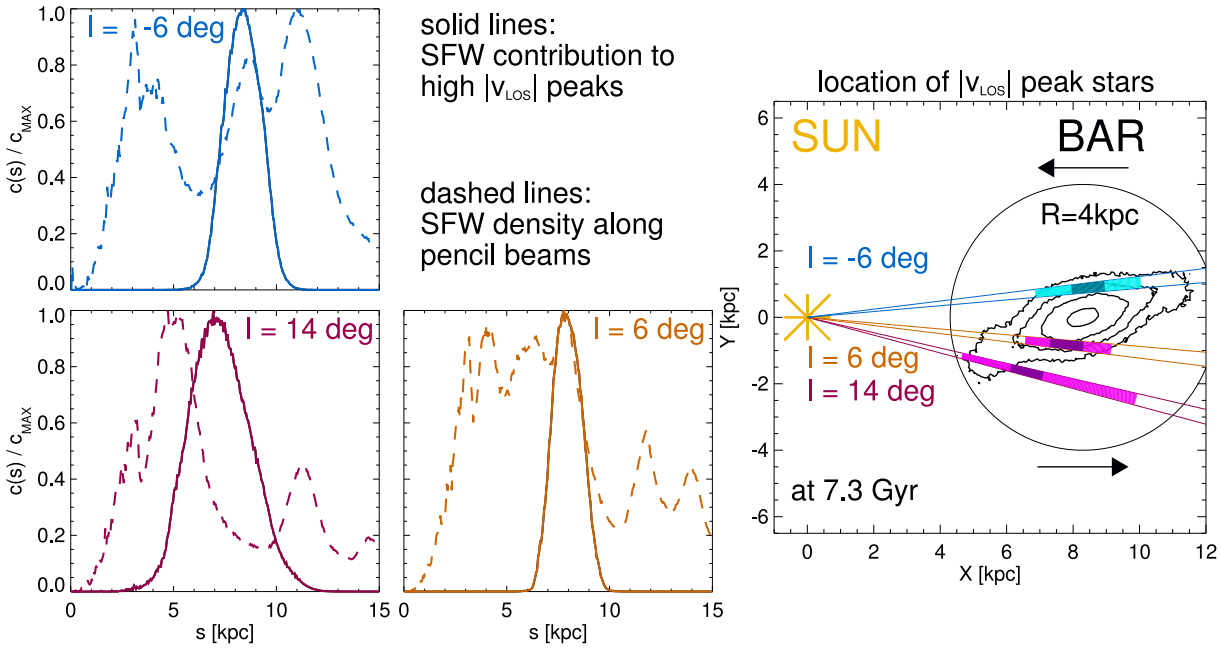

Figure 8. Left-hand panels: the SFW distribution of all stars in a sightline (dashed lines) and of the stars contributing to the high $|v_{\rm los}|$ peaks (solid lines) as a function of their distance from the Sun s, $c(s)/c_{\rm max}$. We show longitudes $l = 14 \pm 1$ (red), $l = 6 \pm 1$ (orange) and $l = -6 \pm 1$ (blue) deg. High $|v_{\rm los}|$ windows are defined as $180 < v_{\rm los}/\,{\rm km\,s^{-1}} < 250$ for $l = 14 \pm 1$, $220 < v_{\rm los}/\,{\rm km\,s^{-1}} < 280$ for $l = 6 \pm 1$ and $-300 < v_{\rm los}/\,{\rm km\,s^{-1}} < -200$ for $l = -6 \pm 1$, as indicated in Fig. 7. Right-hand panel: the location of the high $|v_{\rm los}|$ peak stars in the $x - y$ plane. We show the general geometry of single sightlines from the Sun (yellow star) into the bar (stellar mass density contours from Fig. 3 in black). Arrows indicate galactic and bar rotation. The black circle marks $R = 4$ kpc. The magenta areas show the distance areas which contain 95 per cent of the SFW stars contributing to the high $|v_{\rm los}|$ peak windows for stars moving away from the Sun, cyan areas are for high $|v_{\rm los}|$ stars moving towards the Sun at negative longitudes. Darker shaded areas show the areas of ± 0.5 kpc centred on the peaks of $c(s)$. Note the position of the fast moving stars with $180 < v_{\rm los}/\,{\rm km\,s^{-1}} < 250$ at $l = 14$, which indicates the increasing contribution of stars outside the bar.

at a galactocentric radius $R \sim 4$ kpc and thus at distances $s \sim 4$ and 12 kpc are visible as local maxima. Moreover, spiral structure creates minor peaks.

The high $v_{\rm los}$ feature appears connected to young bar stars. To verify this assumption, we plot in the left-hand panels of Fig. 8 the contribution to the high $|v_{\rm los}|$ features of SFW stars for the three sightlines of Fig. 7 as a function of distance from the Sun s (solid lines). The intervals we use as definitions for these features are indicated by dotted vertical lines in Fig. 7. For $l = \pm 6$ deg, we were guided by the distinctly visible feature, for $l = 14$ deg, where we find no feature, we use the estimate by Nidever et al. (2012).

At each sightline in Fig. 8, the regions of contributions to the high $|v_{\rm los}|$ stars are much narrower than the SFW distribution of all stars in the pencil beam. Moreover, the maxima of contribution to the high $|v_{\rm los}|$ stars are (apart from $l = 6$ deg) offset from the maxima of the SFW distribution of all stars. The distance distribution of contributing stars $c(s)$ is narrowest for $l = 6$ deg and widest for $l = 14$ deg. The main peaks are at $s = 7$–8.5 kpc on the rear side of the bar (front side for $l = -6$ deg). To visualize where these contributions arise in relation to the bar, we use the right-hand panel of Fig. 8, where we show the position of the Sun in yellow, the considered sightlines in blue, red and orange and the surface

density contours of the stellar mass in the bar region at 7.3 Gyr in black (see Fig. 3). The 95 per cent contribution regions of high $|v_{\rm los}|$ stars for each sightline are shown in magenta for stars moving away from the Sun and in cyan for stars moving towards the Sun at negative longitudes. We highlight the regions of ± 0.5 kpc around the peak distances in darker shades. For $l = \pm 6$ deg, these regions are fully within the bar region and strictly on one side of the bar (rear side for $l > 0$, front for $l < 0$), as the fast stars travelling alongside the bar have to lose angular momentum on the way in and gain it on the way out. The contribution region is narrower for $l = 6$ deg as this sightline crosses the bar at a greater angle than the one for $l = -6$ deg.

This indicates that the high $|v_{\rm los}|$ features found by Nidever et al. (2012) correspond to stars which are associated with the bar region and not with disc orbits. This confirms the ideas of Nidever et al. (2012) and Molloy et al. (2015) and rejects the notion of Li et al. (2014) that the observed features are not related to the bar.

At $l = 14$ deg there is a tentative feature in observed data, but not in our simulations. If we select the highest $v_{\rm los}$ stars in the simulation we find that the main contributions come from the edge of the bar, but extend far into the disc region behind the bar. At these longitudes, the inner parts of the disc align with the line of sight and start to contribute to the high $v_{\rm los}$ window. Should the high $v_{\rm los}$ feature at $l = 14$ deg prove to be real, a clear attribution may only be possible with detailed analytical models.

6.2 Detailed comparison with APOGEE

We now directly compare our model with APOGEE data. Remember that we have done nothing at all to fit this specific model galaxy to the MW. There may be significant differences in length, mass, age and detailed history of the bar etc. Hence the goal is to qualitatively identify features and not to do a full quantitative analysis.

In Fig. 9 we compare $v_{\rm los}$ histograms for all stars along the sightlines, equally weighted (EW, green) or selection function weighted (SFW, black) to the APOGEE data described in Section 2 for various sightlines. We display in-plane data at $|b| < 1$ deg in the upper two rows, and sightlines at higher $|b|$ in the bottom two rows. Despite its limitations, the simulation fits the data surprisingly well. The SFW models provide a better fit to APOGEE data than the EW models. Their high $v_{\rm los}$ features are more distinct and the EW histograms are offset from the data at large l as well as at large b.

The sightlines with $l \gtrsim 14$ deg are increasingly dominated by disc stars. There, the parts aligned with the line of sight would bury any distinct velocity feature from the bar. In concordance with this expectation, there is no discernible feature in the corresponding in-plane APOGEE data, and also not in the model. In contrast, at $l = 3$–10 deg, the high-velocity feature is prominent both in the MW data and our simulation. Taking into account the significant Poisson noise in the observations, there is little difference at $l \leq 6$ deg. At $l = 10$ deg, the feature is less distinct in the simulation. Interestingly, at $l = 16$ deg the SFW histogram provides a worse fit than the EW histogram, as it misses the position of the main peak, which at other longitudes is well reproduced.

When we look slightly above and below the plane at $|b| = 1$–3 deg, asymmetries at high $v_{\rm los}$ are present in APOGEE data at $l = 5$–15 deg, but again not at greater l. The tentative $l = 14$ peak in the data was highlighted by Nidever et al. (2012), but has a very weak counterpart in the simulation. The SFW model histogram here drops less steeply than the data on the high-velocity side of the main peak, as is the case for $l = 16$ deg (mentioned above). These are the strongest discrepancies between model and observations. There may be various explanations for this.

(i) We know that the Galactic potential will not be perfectly matched. In particular for disc contributions, the location of the main $v_{\rm los}$ peak is determined by the radial potential gradient (in idealization the circular speed). If this differs, simulation and data will show a systematic difference. (ii) We know that the structure in particular in this region will show differences between simulation and observed data, e.g. caused by a difference in bar length. A longer bar would mean that we see regions further away from the bar tips. We can achieve such an effect also by lowering the solar radius. Indeed, if we do so, the asymmetry becomes more prominent. (iii) Another explanation could be the dense ring of molecular clouds at $R = 4$ kpc in the MW (Dame et al. 1987). This ring is associated with an intense radial peak in star formation, which is not matched by our simulations. The selection function of APOGEE is very sensitive to young stars. This feature will have no strong consequence when the sightline is perpendicular to circular orbits at $R \sim 4$ kpc (at small l) or outside the region ($l \gtrsim 30$), but sightlines at $l \sim 16$ deg will be strongly affected. As they pass through $R = 4$ kpc at an intermediate angle to the local azimuthal direction, the enhancement of these stars will drive up stellar densities at intermediate $v_{\rm los}$ and shift the main peak. Overall, the complicated contribution function of stars at these sightlines prevents any strong conclusions to be drawn from this discrepancy.

Moving even further away from the plane, we consider latitudes $|b| \geq 3$ deg in the lower row of Fig. 9. There is no discernible feature, either in observations or simulation. The slight asymmetry is linked to the rotation of the bar. So our model provides reasonable fits to the data in and out of the plane.

6.3 Varying the parameters

We now examine the behaviour at different latitudes. Fig. 10 shows simulation data for two sightlines $l = \pm 6$ deg and varying latitude. We do this both for SFW histograms for all stars along the lines of sight (left-hand panels) and for EW young central stars (right-hand panels). The difference between these two types of histograms is even more striking at higher $|b|$ where for young central stars they are significantly broader. This indicates that young bar stars play a small role in observations at higher latitude. Note also that the number of young bar stars decreases strongly with increasing latitude in the simulations, which explains the noisier nature of the corresponding histograms. We find that the exponential scaleheight h_z for stars with ages <2 Gyr, which contribute to the high $v_{\rm los}$ features is $h_z \sim 70$–80 pc, compared to $h_z \sim 180$ pc for all stars at the ends of the bar.

All panels show that distinct high $|v_{\rm los}|$ features are only present close to the plane. At $|b| = 1$–2 deg a mild feature is still present, while at greater b there is nothing left. This explains why Zoccali et al. (2014) did not discover such features in their data, which are mostly at $|b| \geq 2$ deg. Their only field at smaller latitude is at $l = 0$, where we do not expect a peak anyway. This can be explained by the fact that the high $v_{\rm los}$ populations are dynamically cool and thus also live at small vertical distances from the Galactic plane.

So far, we have assumed a bar angle of $\phi = 20$ deg. In the literature, estimates range from 15 to 40 deg. Molloy et al. (2015) recently claimed that the high $v_{\rm los}$ features observed by Nidever et al. (2012) could help to constrain ϕ and would favour low values $\phi \sim 15$ deg. In Fig. 11, we thus attempt to study the influence of ϕ on $v_{\rm los}$ distributions. We consider angles between 10 and 55 deg

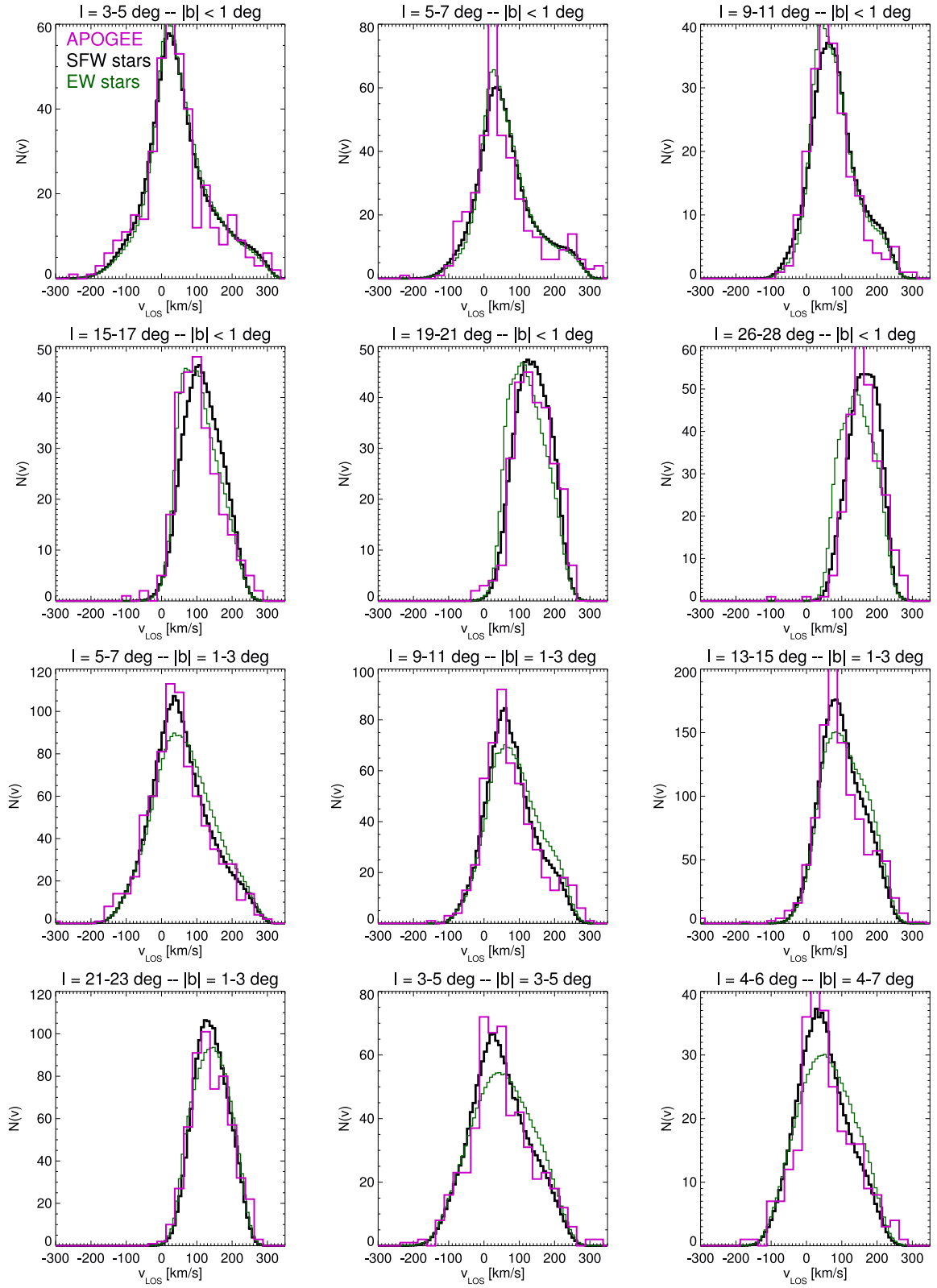

Figure 9. A comparison with APOGEE data. For 12 sightlines for which data from APOGEE are available we compare line-of-sight velocity $v_{\rm los}$ distributions $N(v_{\rm los})$ to the data discussed in Section 2. The APOGEE data show the actual number of stars per bin, the simulation data are normalized to yield the same total number. The APOGEE $v_{\rm los}$ bins are 25 km s^{-1} wide, whereas the simulation bins are 8 km s^{-1} wide. For comparison to APOGEE data (magenta), we show simulation histograms for equally weighted (EW, green) and selection function weighted (SFW, black) stars along the sightline. We assume a bar angle of $\phi = 20$ deg and a solar radius of $R = 8.3$ kpc.

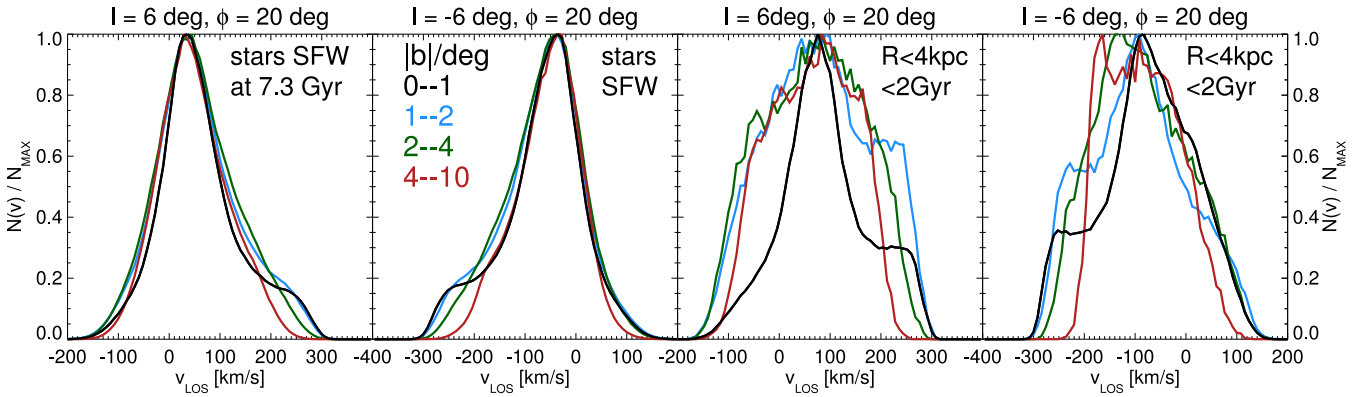

Figure 10. Line-of-sight velocity $v_{\rm los}$ distributions $N(v_{\rm los})/N_{\rm max}$ as seen from $R = 8.3$ kpc at a bar angle of $\phi = 20$ deg at a simulation time of 7.3 Gyr. $v_{\rm los}$ bins used here are all 8 km s^{-1} wide. We consider sightlines centred on $l = \pm 6$ deg, which are both 2 deg wide in l. In each panel, we consider four latitude bins: $|b| < 1$ deg (black), 1–2 deg (blue), 2–4 deg and >4 deg (red). Left-hand panels: here we consider histograms of all stars along the sightline, weighted by the selection function depicted in Fig. 1. Right-hand panels: here we consider equally weighted, young stars (ages <2 Gyr) at $R < 4$ kpc.

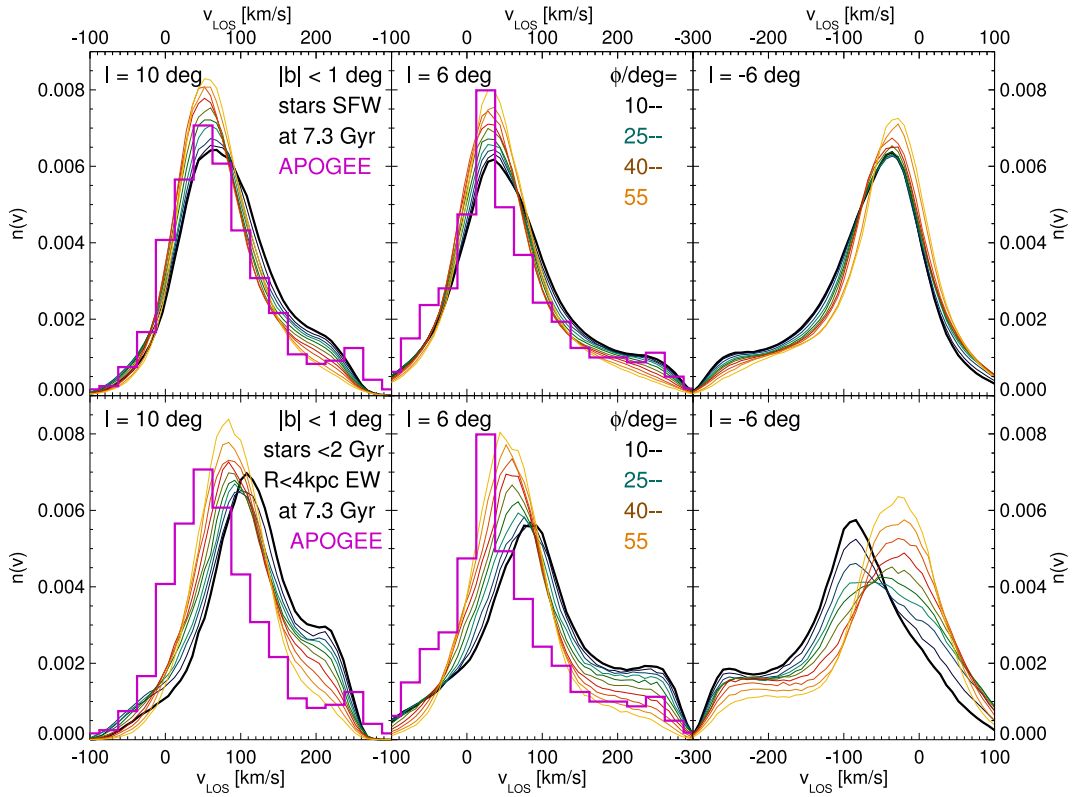

Figure 11. Normalized line-of-sight velocity $v_{\rm los}$ distributions $n(v_{\rm los})$ of stars at 7.3 Gyr simulation time and latitudes $|b| < 1$ deg assuming a solar radius $R_{\rm sun} = 8.3$ kpc. If available APOGEE data are overplotted in magenta. In each panel, we consider bar angles ϕ between 10 and 55 deg. Upper row: all stars in the sightline, weighted by the selection function presented in Fig. 1. Lower row: all stars within $R < 4$ kpc and with ages <2 Gyr, equally weighted. Left-hand column: longitude $l = 10 \pm 1$ deg. Middle column: longitude $l = 6 \pm 1$ deg. Right-hand column: longitude $l = -6 \pm 1$ deg.

for three sightlines and both SFW stars (upper row) and young stars with $R < 4$ kpc (lower row).

We see that both for positive and negative l, the high $|v_{\rm los}|$ features are less distinct for large ϕ. This can be explained by the larger angle between the sightline and the bar. As the high-velocity stars move along the bar, their projected $v_{\rm los}$ decreases. At larger ϕ, stars on different orbits moving at greater angles to the bar can be seen at higher $v_{\rm los}$. As they are less numerous, the feature becomes less prominent. This is especially clear for young stars at $R < 4$ kpc. If one tried to fit multiple Gaussians to the $v_{\rm los}$ distribution, as did Nidever et al. (2012) and Molloy et al. (2015), one would find that the high $v_{\rm los}$ peak becomes broader and centred at lower $v_{\rm los}$ as reported by Molloy et al. (2015).

In the upper panels of Fig. 11, APOGEE data are plotted over the SFW model. We should keep in mind the uncertainties in the observations and the fact that the structure and age distribution of the model bar differ in an unknown extent from the MW bar. We thus conclude that the APOGEE data put only mild constraints on the bar angle. They favour small angles, but only strongly disfavour angles $\phi \gtrsim 40$ deg.

The estimate by Molloy et al. (2015) is also intrinsically overly confident, as they ascribe the high v_{los} feature to one orbit family only, whereas, as we will show in the next section, several families can contribute. Moreover, degeneracies with the potential, the pattern speed, the bar structure etc. complicate their determination of ϕ.

7 TRACKING ORBITS

To understand better the origin of the high and low v_{los} peaks discussed above, we focus in this section on the orbits producing these features. All orbits in this section are analysed in a rotating reference frame, which corotates with the bar.

7.1 High and low v_{los} features

We created snapshots of the simulations at a frequency of 1 per 1 Myr from simulation time 7.3 Gyr onwards. We first consider the following exercise: What would the v_{los} distribution look like if it were only made up of stars that at some point contribute to the high v_{los} peak. We therefore select all stars with ages <2 Gyr and $R <$ 4 kpc that at 7.30–7.35 Gyr contribute to the high v_{los} peak at $l = 6 \pm 1$ deg and $|b| < 1$ deg. We then follow these particles for a further 500 Myr and construct a v_{los} distribution at the same l and b ranges only from these stars. We do the same 2 Gyr later for a new set of stars selected in the same way. Figs 6 and 5 have already shown that the maximum (minimum) v_{los} observed increase (decrease) by about 20 km s^{-1} within these 2 Gyr. This is because of a growth of both the potential well and the bar and also because of the slowdown of the bar which allows orbits to have lower angular momentum and reach positions closer to the centre and thus cover a larger potential difference. Consequently, we increase the high v_{los} window from $210 < v_{los}/\,\mathrm{km\,s^{-1}} < 280$ to $230 < v_{los}/\,\mathrm{km\,s^{-1}} < 300$.

These v_{los} distributions are shown in Fig. 12. Unsurprisingly they have their main peaks at the selection positions. Both distributions clearly show a distinct peak at negative v_{los} made up by orbits returning along the other side of the bar. This peak was already visible in Fig. 6 for 9.3 Gyr. The increase in maximum absolute velocities between 7.3 and 9.3 Gyr widens the gap between the peaks and shifts the main peak of the overall distributions for stars within $R < 4$ kpc to higher v_{los}. Consequently, the negative v_{los} peak at 9.3 Gyr for Fig. 6 becomes visible. The negative peak comprises approaching stars, while the positive peak features stars moving away from the Sun. Fig. 12 reveals a third peak for 7.3 Gyr indicating that a group of orbits has a more complicated structure than alternately contributing to the two peaks.

In the right-hand panel of Fig. 12, we visualize the origin of the high and low v_{los} peaks at $230 < v_{los}/\,\mathrm{km\,s^{-1}} < 300$ and $-150 < v_{los}/\,\mathrm{km\,s^{-1}} < -50$ for young bar stars at 9.3 Gyr from spatially separate components along the line of sight. Here, we plot the spatial positions of all stars in the positive v_{los} peak at 9.3 Gyr in black and of all stars in the negative v_{los} peak at 9.3 Gyr in red. The components clearly separate to the expected sides. One orbit family that would contribute to both peaks are the x_1 orbits. In the rotating frame of the bar, these orbits move along opposing sides of the bar major axis and turn around at the bar tips. They would obviously produce the two peak feature in the left-hand panel of Fig. 12, as was e.g. discussed by Molloy et al. (2015). We overplot in green one such orbit extracted from the simulation which alternately contributes to both peaks. However, as we will show below, the high v_{los} features in our simulation are made up of a more complicated population of orbits from different orbit families.

7.2 A simple classification for high v_{los} orbits

To get a better understanding for the orbits that contribute to the peak, we track all orbits that contribute to the high v_{los} peak at $l = 6 \pm 1$ and $|b| < 1$ deg at 7.30–7.35 Gyr defined by $210 < v_{los}/\,\mathrm{km\,s^{-1}} < 280$ for young stars with ages <2 Gyr and radii $R < 4$ kpc. If an orbit is similar to a closed orbit, we will expect it to return to the same region in phase space periodically. Our selection of sightline plus v_{los} range can be seen as a rough proxy for a phase space region. Considering that the bar grows and the potential changes, a more sophisticated definition is complicated. Therefore, we record

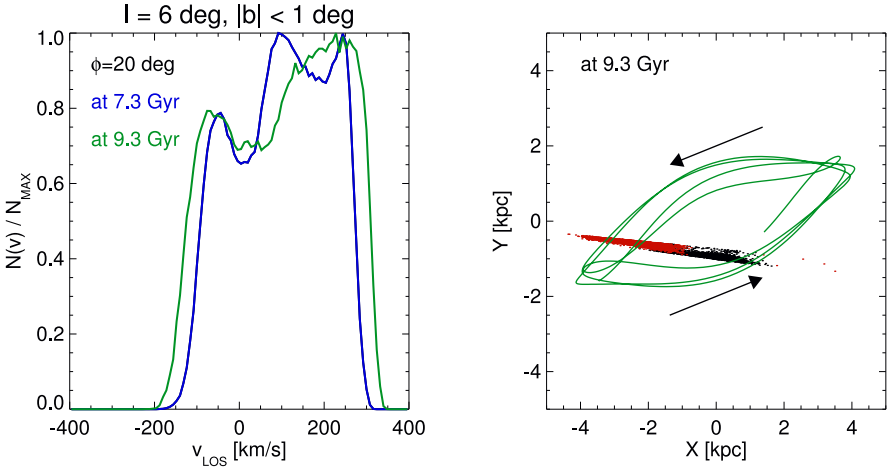

Figure 12. Left-hand panel: line-of-sight velocity v_{los} distributions $N(v_{los})/N_{max}$ of young stars at $R < 4$ kpc as seen from $R = 8.3$ kpc with a bar angle $\phi = 20$ deg at longitudes $l = 6 \pm 1$ deg and latitudes $|b| < 1$ deg. The stars were selected as members of the high-velocity peaks, defined by $210 < v_{los}/\,\mathrm{km\,s^{-1}} < 280$ at 7.30–7.35 Gyr (blue) and by $230 < v_{los}/\,\mathrm{km\,s^{-1}} < 300$ at 9.30–9.35 Gyr (green). Then they were followed for 500 Myr with a snapshot separation of 1 Myr and each time they were in the sightline $l = 6 \pm 1$, their v_{los} was recorded to produce the shown v_{los} distributions. Right-hand panel: the positions of stars at 9.30–9.35 Gyr seen at longitudes $l = 6 \pm 1$ deg and latitudes $|b| < 1$ deg and either in the high v_{los} peak ($230 < v_{los}/\,\mathrm{km\,s^{-1}} < 300$, black dots) or the low v_{los} peak ($-150 < v_{los}/\,\mathrm{km\,s^{-1}} < -50$, red dots). Each star is recorded only once, on its first detection in the corresponding velocity window. The Sun is at $x = -8.3$ kpc and $y = 0$ here. Overplotted in green is an orbit over 500 Myr, which during this time alternately contributes to both peaks. The arrows indicate the sense of motion.

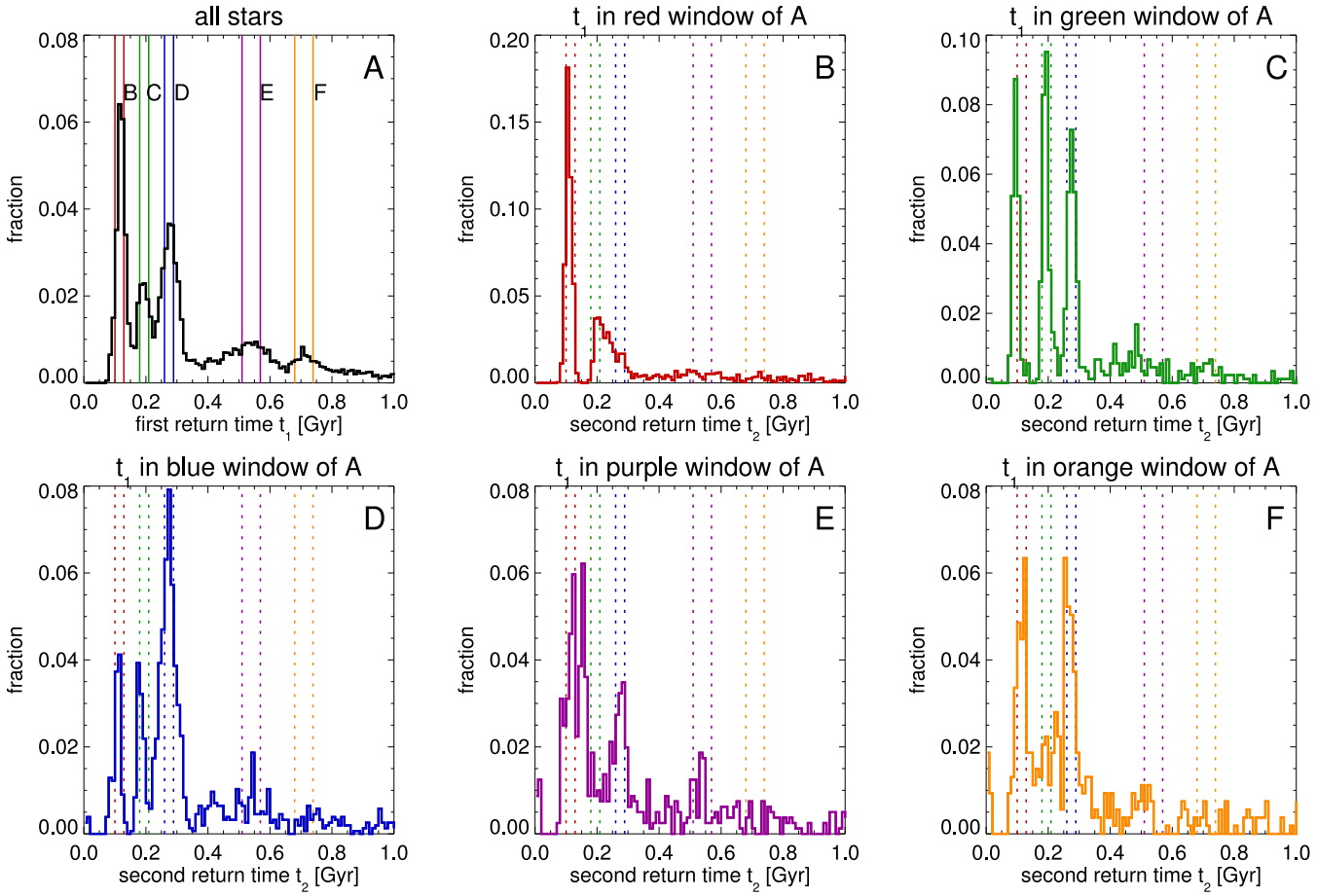

Figure 13. For this figure, we track stars which at 7.30–7.35 Gyr are younger than 2 Gyr and at galactocentric radii $R < 4$ kpc, and contribute to the high $v_{\rm los}$ peak ($210 < v_{\rm los}/\,{\rm km\,s^{-1}} < 280$) at $l = 6 \pm 1$ and $|b| < 1$ deg. We track them for 2.4 Gyr afterwards. We record the first, second and third time (τ_1, τ_2 and τ_3) at which they are at $l = 6 \pm 1$ and $210 < v_{\rm los}/\,{\rm km\,s^{-1}} < 280$ and use it to calculate the first and second return time intervals $t_1 = \tau_2 - \tau_1$ and $t_2 = \tau_3 - \tau_2$. Panel A: the histogram for t_1. The peak selection windows are marked by vertical lines in red, green, blue, purple and orange. Panels B–F: t_2 histograms for orbits selected to be in one of the t_1 peak windows marked in panel A. The colour of each panel corresponds to the colour of the selection window. The selection windows from panel A are marked by dotted vertical lines.

the time interval needed by an orbit to return to the sightline and $v_{\rm los}$ window. The histogram for the first return time t_1 is plotted in the panel A of Fig. 13. We see that this distribution shows three distinct peaks at circa 110 (red), 190 (green) and 280 Myr (blue), which contain approximately 23, 13 and 28 per cent of the stars. There are also two broader peaks at 450–650 Myr (14 per cent, purple) and 650–800 Myr (7 per cent, orange). Note that $\sim$ 13 per cent of orbits never return or have return times $>$ 800 Myr. Were all these orbits simple x_1 orbits, we would expect a simpler structure.

In panels B–F of Fig. 13, we look at histograms of the second return time t_2 for stars selected to have first return times t_1 in the five peaks found in the t_1 histogram. To some degree, all these t_2 histogram resemble the t_1 histogram, as they reproduce one to three of the previously found three narrow peaks. Above 450 Myr, the t_2 histograms all seem dominated by noise, but all of them contain a similar fraction of such orbits, varying between 25 and 31 per cent. A first clear conclusion is, that for each histogram, the fraction of orbits that remain in the same return time peak is below 50 per cent. This shows that most orbits do not show a steady periodicity in our definition, but rather combine a low number of possible return times.

To connect the shape of these histograms to types of orbits, we extracted random sets of orbits with similar combinations of return times t_1 and t_2, for example contributors to the green peak for t_1 and to the blue peak for t_2. In addition, we extracted a set of orbits that do not contribute to return time peaks. From these we select by eye 42 typical orbits. They are shown in Fig. 14. Note that due to different prominence of the peaks this figure does not represent orbit types at their underlying contribution fractions.

The stars with shortest return times t_1 (red peak) show a high fraction (45 per cent) of stars with $t_1 \approx t_2$. Additionally, 30 per cent of the stars have t_2 in the area of the green or blue peak, but these peaks are not separately visible. The first row of Fig. 14 reveals that these stars are essentially all on x_1 like orbits. If they have $t_2 \gg t_1$, it is mostly because the orbits are not exactly closed. They can miss the high $v_{\rm los}$ window as their directions of motion and velocity vary when they cross the sightline. Moreover, N-body noise can cause the integrals of motion of the particles to fluctuate.

Stars from the second (green) t_1 peak show three t_2 peaks at the locations of the three narrow t_1 peaks which are equally populated ($\sim$25 per cent each). Most stars are again on x_1-like orbits, but there are also the first objects from more complex closed orbit families with Pretzel-like structures (Portail, Wegg & Gerhard 2015b), such as the 202-213 or 216-229 objects. At higher return times, x_1 orbits are a minority. If they have such long return times, it is because they miss $v_{\rm los}$ due to the fluctuations mentioned above more often than

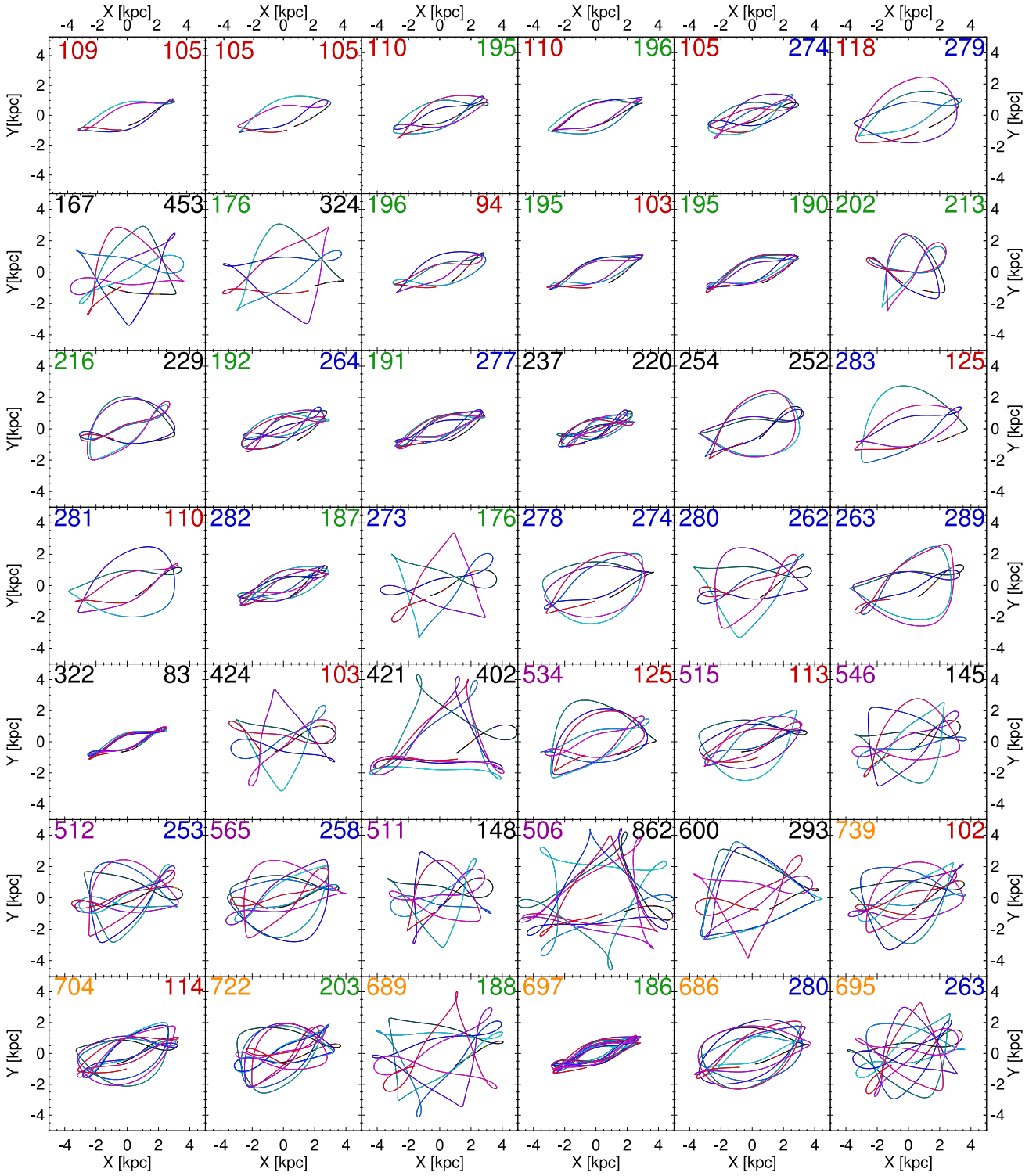

Figure 14. 42 orbits in the $x - y$ plane of particles that at 7.3 Gyr contribute to the high $v_{\rm los}$ peak at $l = 6 \pm 1$ deg. The orbits are shown from when they first leave the sightline until the second time they return to the sightline and contribute to the high $v_{\rm los}$ peak again. The numbers in the corners of the panel indicate the times between contributions to the peak in Myr. If these fall into one of the return time peaks identified in Fig. 13 they are coloured accordingly, if they do not, they are coloured black. The orbit colour coding indicates time, changing from black via light and dark blue to red with increasing time. Orbits are shown in the frame corotating with the bar.

not, e.g. because they have lower energies and only in exceptional cases reach high enough $v_{\rm los}$.

Pretzel-like morphologies are the most frequent pattern found at longer return times. For blue t_1 stars, there is again a high fraction (46 per cent) of $t_1 \approx t_2$ stars, which tend to shows such patterns, as seen in the fourth row of Fig. 14. Generally, the structures become more complicated and more irregular as t_1 increases. Clearly some orbits show 3:1 characteristics with a changing orientation (objects

421-402 or 506-862), but there are also more complicated, but apparently regular structures, such as the object 273-176, which was labelled 'Q' in Voglis, Harsoula & Contopoulos (2007), and objects like 176-324 or 424-103 which also combine 3:1 and x_1 features. Other orbits appear to change structure with time, an indication of chaotic behaviour.

If we combine the results from above, we estimate that the fraction of stars in the high v_{los} peak that are on x_1 orbits at the given time is between 40 and 50 per cent. If we determined the full population of stars, which over a longer time-scale (∼1 Gyr) periodically contributed to the high v_{los} peak, the fraction of x_1 stars would be even lower, as they have the shortest return times. This invalidates the original assumption of Molloy et al. (2015) that the high v_{los} feature is only caused by 2:1 orbits. There are other major contributors, most prominently the Pretzel-like orbits, but also 3:1 or more complex orbits. We note that Molloy et al. (2015) have recently updated their paper in response to our work and now also find that higher order orbit families (they name 3:1 and 5:2) can make significant contributions to the high v_{los} features.

We note that we have attempted to analyse the vertical structure of orbits in connection to the in-plane one and experimented with frequency analysis, but concluded that the results were too diverse or noisy to help with the understanding of the high v_{los} features.

7.3 Are orbits evolving away from high v_{los} orbits?

In our discussion of Fig. 13, we already noted that around 10 per cent of stars which contribute to the high v_{los} peak at a given time and sightline, need 1 Gyr or longer to achieve this again. The t_2 histograms have also shown that ∼25 per cent of stars that initially had return times <400 Myr need more than 500 Myr to return again. So orbit populations slowly change in a way that reduces the proportion of their time during which they contribute to the high v_{los} peak.

To understand why the high v_{los} peak vanishes with age, we conducted the following exercise. We tracked all orbits from the histogram in panel A of Fig. 13. As the orbits that never return or have very long return times (defined as > 0.8 Gyr) are likely random contributors, we exclude them. We record each passage of the sightline (total number $N_{window}(t)$) and if during this passage the orbit contributes to the high v_{los} peak (total number $N_{peak}(t)$). The fraction $\nu = N_{peak}(t)/N_{window}(t)$ gives a measure of how much the population of orbits is contributing to the peak at time t. A priori one would expect a ratio $\nu \sim 0.5$ for x_1 orbits as they are approximately axisymmetric along the bar passing once through the sightline while approaching and once while moving away and contributing to the high v_{los} peak. Consequently, smaller values for ν are expected for more complex orbits. This is slightly complicated by the geometry and the slower absolute velocity of stars while approaching: The front side of the bar is geometrically disfavoured, as the pencil beam covers a larger area at the rear side. On the other hand, the approaching stars are closer to the tip and hence slower, taking more weight in the observations. Moreover, it is also possible that stars moving along the rear side have high enough v_{los} only for a fraction of the time they spend in the sightline. If we select x_1 orbits which at every second crossing of the sightline contribute to the high v_{los} peak, we empirically find a mean value of $\nu \approx 0.45$, close to the simple estimate.

From the return time analysis shown above, we would expect $\nu < 0.45$, as most orbits exhibit a more complex behaviour. $\nu(t)$ is shown in Fig. 15. Initially, ν fluctuates periodically. This can be understood as most orbits return to the high v_{los} peak after specific

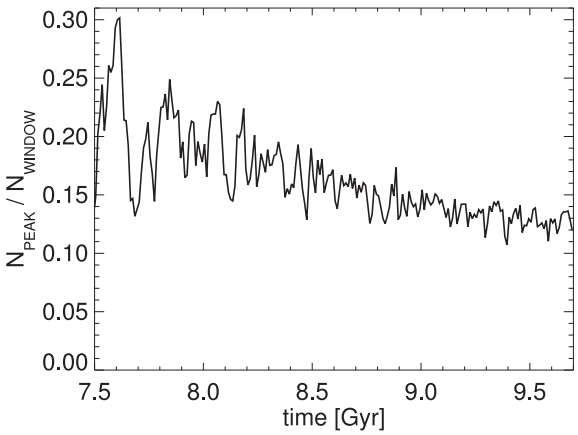

Figure 15. For this figure, we track all orbits from the histogram in panel A of Fig. 13. We exclude orbits that never return to the high v_{los} window or have very long return times $t_1 > 0.8$ Gyr. We record each passage of the sightline $l = 6 \pm 1$ deg (total number $N_{window}(t)$) and each contribution to the high v_{los} peak $210 < v_{los}/\,\mathrm{km\,s^{-1}} < 280$) during such a passage (total number $N_{peak}(t)$). We plot the fraction $\nu(t) = N_{peak}(t)/N_{window}(t)$.

characteristic times (see Fig. 13) and they have been selected at correlated phases. The average value of ν over the covered 2 Gyr drops from $\nu \sim 0.22$ to $\nu \sim 0.12$. This shows that the fraction of orbits contributing to the high v_{los} peak continuously decreases.

Most of this decrease is caused by diffusion of stars away from the contributing orbits, but it is not clear, if our simulation handles this diffusion correctly. Sources for this diffusion are chaotic orbit behaviour, two-body noise and fluctuations in bar parameters. Our resolution is likely not sufficient to cover chaotic orbital behaviour correctly. For the two-body noise, it is unknown if the level of N-body noise is realistic compared to the MW (bearing e.g. giant molecular clouds near the bar tips, and dark matter substructure). In addition, our simulation will not have sources for bar fluctuations like tidal torques exerted by satellites.

The important point to take away is that the vanishing of the high v_{los} peak in older stars is not only due to the broadening of the main peak, but also due to active loss of stars from high v_{los} orbits.

7.4 Orbit capture by the bar

By design, new-born star particles in our simulation are released on near circular orbits, where the circular speed was determined to balance the local radial component of the gravitational force. Obviously, the young stars contributing to the high v_{los} peak discussed above are not on circular orbits. Just as obviously, there are no stable circular orbits near the bar. This is why we set an inner radius limit for new born stars, so that no new star particles are inserted within the main bar region. This cutoff is, of course, to some degree arbitrary and young stars born close to the bar can be captured by the bar, resulting in the young bar populations studied in the previous sections. Bars in real galaxies can also grow by capturing stars and thus changing their orbits. So the young stars that end up in the high v_{los} peak are predominantly the result of continuous bar growth.

In Fig. 16, we show six stars that at 8.3 Gyr contribute to the high $v_{los} > 220\,\mathrm{km\,s^{-1}}$ feature and were born within 1 Gyr before that time. We find that the shortest time it takes to appear in the high v_{los} peak is similar to the shortest return time peak, 110 Myr. The capture times are rather equally distributed between this lower limit and the maximum 1 Gyr due to the selection criteria. The shown star particles were selected at different *capture time* intervals. They

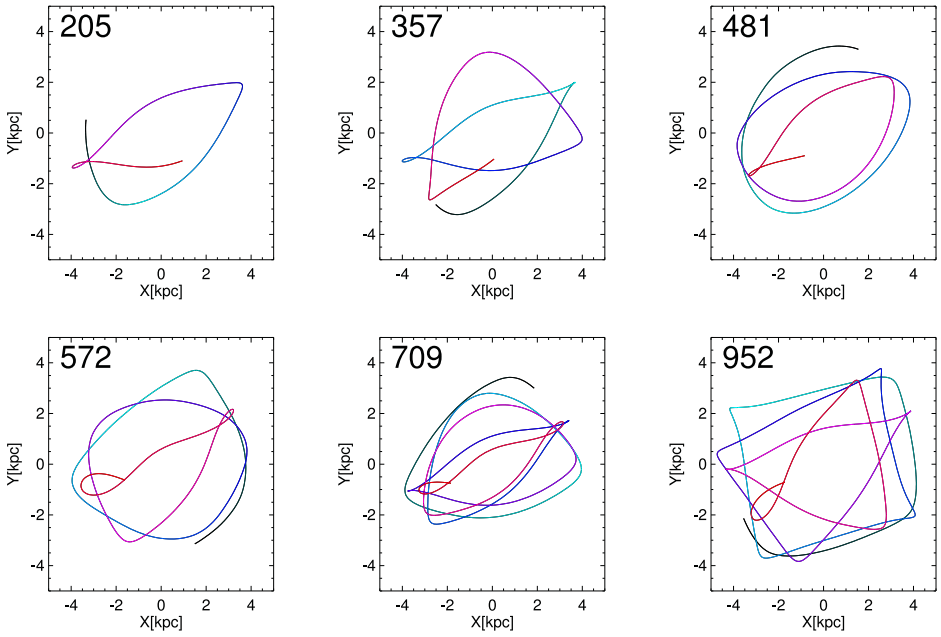

Figure 16. Orbits of captured particles in the $x - y$ plane. These stellar particles are born between 7.3 and 8.3 Gyr and contribute to the high $v_{\rm los} > 220\,{\rm km\,s^{-1}}$ feature at $l = 6 \pm 1$ deg and 8.3 Gyr. The numbers in the top-left corners indicate the time in Myr between birth and first detection in the high $v_{\rm los}$ window at $l = 6 \pm 1$ deg. The colour coding indicates time, from black at birth via light and dark blue to red at first detection. Orbits are shown in the frame corotating with the bar.

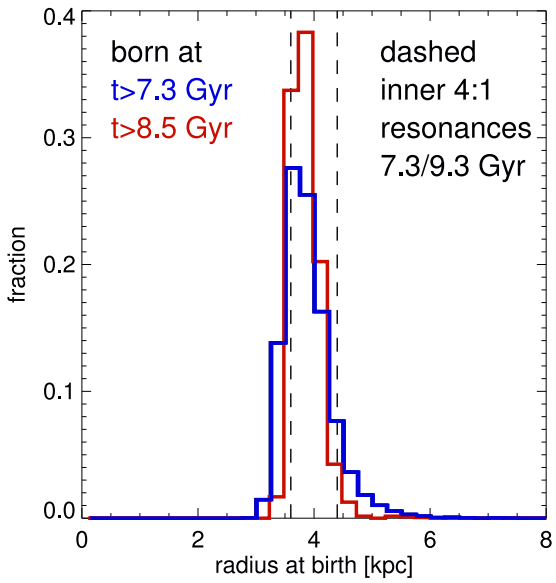

Figure 17. For this figure, we select stars which were born after 7.3 Gyr and at 8.3–8.5 or at 9.3–9.5 Gyr contribute to the high $v_{\rm los}$ window at $l = 6$ deg. The union of the samples found at these two time intervals comprises ∼11 000 stars. The distribution of birth radii $R_{\rm birth}$ of all ∼11 000 stars is shown in blue. The histogram of stars born after 8.5 Gyr and contributing at 9.3–9.5 Gyr is shown in red. The vertical dashed lines mark the positions of the inner 4:1 (ultraharmonic) resonance at 7.3 and 9.3 Gyr.

start out on non-bar orbits and at some point transition to x_1-like or Pretzel-like orbits.

Clearly, stars that end up in the high $v_{\rm los}$ features are born at radii that correspond to the tip of the bar, so they belong to the innermost inserted particles. To visualize this point, we plot in Fig. 17 the distribution of birth radii $R_{\rm birth}$ of high $v_{\rm los}$ stars. For this figure, we select stars which were born after 7.3 Gyr and contribute to the high $v_{\rm los}$ feature at $l = 6$ deg at 8.3–8.5 Gyr and/or at 9.3–9.5 Gyr. The union of the samples found at these two time intervals comprises ∼11 000 stars, for which we determine birth radii. The histogram for all stars is shown in blue, the one for the subsample of stars born after 8.5 Gyr is shown in red. We notice that the majority of stars is born just outside the bar at $R \sim 4$ kpc. As seen in Fig. 2, the bar radius fluctuates mildly, which allows smaller birth radii. The subsample of stars which were born at later times has its lower cutoff slightly further out due to the continuing growth of the bar. The outer tail is wider for older stars, indicating that stars which are older at capture can have larger birth radii. This is because they had more time to migrate radially inwards.

Resonances can play a role in capturing orbits (e.g. Binney & Tremaine 2008). The corotation resonance of our bar at the analysed time intervals is at $R = 7$–9 kpc, but no stars from these regions are captured. We find that the ultraharmonic resonance (UHR), $4(\Omega – \Omega_{\rm bar}) = \kappa$, in our model lies just outside the bar. This is likely not coincidental, as the UHR can limit the radial extent of stable x_1 orbits and thus the size of the bar (Patsis, Athanassoula & Quillen 1997). The resonance may play a role in shaping the spatial distribution from which stars are captured by the bar, as while the bar grows, the resonance moves outwards, and stars on orbits just outside the bar get scattered, absorbed or released by it. These processes can transport orbits to the regions of phase space occupied by high-velocity bar orbits. However, the exact role of the resonance in the capture process is unknown, as the bar is strong, evolving and the potential is not smooth. The capture of orbits can be understood in simpler terms (similar to Lynden-Bell 1979), in that stars come in at the right angle to the bar to lose angular momentum and get trapped. A detailed study of capture processes is beyond the scope of this work.

Capture of stars on to these orbits along the bar is mostly drawn from kinematically cool populations that are close to the galactic plane, which have a small random energy compared to the potential disturbance and are at low altitude, where the disturbance is

strongest. While these stars drastically change the in-plane geometry of their orbits during capture by the bar, their vertical energy and hence scaleheight remain small. Consistently, both the MW and our simulation display a discernible high $v_{\rm los}$ feature only at observed latitudes $b \lesssim 2$ deg.

Above, we have learned that for populations of stars which at a given time contribute to the high $v_{\rm los}$ feature, the contribution fraction slowly declines with time. As the simulation evolves, the high $v_{\rm los}$ feature, however, remains detectable. This is because of ongoing star formation close to the bar region and the continuous capture of young stars on x_1-like or Pretzel-like orbits. The young populations on such orbits then slowly evolve towards more complex orbit populations with a decreasing fraction of high $v_{\rm los}$ stars.

We note that another process which could produce young stars on high $v_{\rm los}$ orbits is not included in our model: in real galaxies, molecular clouds can exist on bar orbits (Sheth et al. 2002). Stars born in these clouds would make up kinematically cool populations born directly on high-velocity bar orbits and could thus contribute to the high $v_{\rm los}$ features.

8 CONCLUSIONS

In this paper, we have studied how an *N*-body+SPH model of a growing MW-like barred disc galaxy compares to the MW in terms of line-of-sight velocities $v_{\rm los}$ of stars seen from the earth and in the direction of the bar. The model uses an approach that has not yet been used in this context. We start with a light (one tenth of the final mass) and short scalelength disc of gas and stars in equilibrium within a live dark halo. This disc is grown by continuously adding star and gas particles on near circular orbits in a controlled way. The mass and size growth histories are matched to expectations for the MW, and indeed at simulation time 7–10 Gyr the simulated bar is similar in structure to the MW bar.

Our simple prescription for the evolution of the galaxy in our *N*-body simulation lowers the computational cost and also circumvents the uncertainties in the parametrization of sub-grid model approaches to star formation and stellar feedback. The general dynamics of gas and stars are expected to be reasonably represented, but we do not cover varying gas fractions, supernova induced turbulence and effects of multiple gas phases. The simulation does not produce any sensible interplay between gas and stars: there is e.g. no enhanced star formation at places with high gas densities. External galaxies show indications for star formation associated with the gas flows along the edges of a bar (the equivalent of the MW's 3 kpc arms; Sheth et al. 2002), which depend strongly on the dynamical state of the bar (see e.g. Friedli & Benz 1995). However, these processes are not covered in our simulation. On the positive side, our approach allows us to set a reasonable star formation history, to keep spurious sources of heating under control, and hence to observe the dynamical effects of bar formation with less scatter.

We use this simulation to interpret line-of-sight velocity ($v_{\rm los}$) data for the central and inner disc regions of the MW from the APOGEE survey. To enable a robust comparison, we apply a simple population synthesis to model the APOGEE selection function. Apart from minor discrepancies at a minority of sightlines, the model fits the data surprisingly well without any scaling or adjustment. The simulation not only reproduces the positions and dispersions of the main peaks in the $v_{\rm los}$ distributions at each sightline, but also displays the high $v_{\rm los}$ features found by Nidever et al. (2012) within the central bar region.

Our simulation clearly identifies these high $v_{\rm los}$ features with stars travelling near the plane alongside the bar. By showing that these are kinematically cool features with preferentially young stars in the plane, we naturally explain why the high $v_{\rm los}$ structure was seen by Nidever et al. (2012) and Babusiaux et al. (2014) in observation fields at $|b| \lesssim 2$, but is absent in the higher-latitude fields studied by Zoccali et al. (2014). By the strong preference of the APOGEE selection function for young stars, the high $v_{\rm los}$ features get additionally enhanced and have comparable strength and shape in our simulation and the APOGEE observations. We also determine at which velocities low $v_{\rm los}$ peaks at negative l, produced by stars moving towards the Sun along the front side of the bar, should be visible. So far, only hints of these features have been seen by Babusiaux et al. (2014).

We show that, unlike for the high $|v_{\rm los}|$ features, the position and width of the main peaks of the $v_{\rm los}$ distributions are dominated by fore- and background stars, which are not associated with the bar. We also study a variation of our parameters, in particular the bar angle ϕ. Other than Molloy et al. (2015) we feel unable to put strong constraints on the observed bar angle: while large $\phi \gtrsim 40$ deg are clearly disfavoured as the majority of high-velocity stars get a too large projection angle with the line of sight, no reliable constraint can be found for smaller values of ϕ, since change in velocities is degenerate with our general uncertainty about the bar length, pattern speed and strength. Additionally, we show that the high $v_{\rm los}$ feature is detectable at simulation times between 7 and 10 Gyr and is thus not connected to specific events. The feature changes mildly over this period due to a growth of the bar in length and mass, but the change is too small to allow any conclusions about the properties of the MW bar.

We note that on two sightlines, namely $l = 14$ and 16 deg, the simulation shows a mild difference to the observations, missing the tentative high $v_{\rm los}$ peak at $l = 14$ and predicting the main peak of the velocity distribution at too high velocities at both sightlines. Possible origins for the discrepancies are a longer bar length for the MW or the 4 kpc molecular ring in the MW. A decisive answer on this question would require detailed analytical models that can cover the full space of possible parameters.

A detailed analysis of the stars participating in the high $v_{\rm los}$ features in our model reveals that (contrary to the original view of Molloy et al. 2015) only about half of the contribution is made by stars on x_1 orbits, with additional large contributions from Pretzel type (Portail et al. 2015b) and more complicated orbits. This finding results from a detailed study of these orbits guided by return times into the high-velocity peak at the sightline $l = 6$ deg. The return times display several peaks that are associated with the different orbit families (and some scatter by stars missing the observation window) and help with the quantification of the contribution of different orbit families. We note that, in response to our work, Molloy et al. (2015) have updated their paper and now also conclude that higher order orbit families (they name 3:1 and 5:2) can make significant contributions to the high $v_{\rm los}$ features.

Another interesting statistic is the ratio of the number of stars in the high $v_{\rm los}$ region of a certain sightline divided by all stars passing through the sightline at arbitrary $v_{\rm los}$ values for all stars that have been observed once in the high-velocity peak. While we find that x_1 orbits with stable short return times show an average ratio of $\nu \approx 0.45$, the stars in the simulation start with a ratio of $\nu \approx 0.22$, as a consequence of the significant contribution of more complex orbits to the velocity peak.

Within 2 Gyr of the initial detection, this ratio drops steadily down to $\nu \approx 0.12$. Due to changes in the bar potential, length, and pattern speed, as well as orbital diffusion, stars diffuse out of these orbit families weakening the high $v_{\rm los}$ peak. However, the high $v_{\rm los}$ feature in our simulation persists, as the growing bar captures new stars from the surrounding disc. It is unclear, how realistically our

model represents the precise balance of orbit capture and diffusion, which is determined by chaotic diffusion, two-body interactions and fluctuations in bar parameters. In addition, observations of enhanced star formation at the bar tips and on bar orbits along the leading bar edges (see above), imply a source of young stars on high-velocity bar orbits, which is not mirrored by our model. Overall, our result provides an indication for the recent growth of the Galactic bar. Quantitative constraints on the bar dynamics and history would demand further exploration of model parameters and also a detailed age and distance tomography of the observed high $v_{\rm los}$ stars.

We note that our bar is a slow bar with $R_{\rm bar} \sim 0.5 R_{\rm CR}$ in a disc with a high dark matter contribution to the circular velocity curve. As discussed in Section 4, observations do not constrain the pattern speed and the length of the MW bar well and we currently can exclude neither a slow bar as ours nor a fast bar with $R_{\rm bar} = 0.7 - 1.0 R_{\rm CR}$. As far as the dark matter fraction is concerned, our disc agrees with recent estimates on the local circular velocity in the MW and the corresponding DM contribution. Further work is necessary to understand how faster bars and/or lower dark matter fractions would alter the processes discussed in this paper.

Debattista et al. (2015) point out that a nuclear stellar disc with a radial extent of $R \sim 1$–1.5 kpc could explain high-velocity features at $l \sim 10$ deg. Although this idea is interesting, they do not currently have a model which can explain the velocity distributions at the full APOGEE range of bar longitudes, as our model can. The simulations of Sormani et al. (2015) advocate against such a giant x_2 disc for the current MW centre, but the extent of such a disc may have varied over time. To safely determine whether this idea can explain the data, a model, which self-consistently predicts velocity distributions at longitudes $l = (-20)$–20 deg would be needed. A higher number of observed stars in this region with reasonable measurements of distances, ages and metallicities would certainly help to (in)validate our model or other attempts to explain the observed velocity distributions. As far as the nuclear stellar disc in the MW is concerned, its existence so far has only reliably been detected in the central 150 pc (Schönrich, Aumer & Sale 2015) and the short scalelength inferred for this structure currently seems to disfavour a large nuclear disc as proposed by Debattista et al. (2015).

To summarize, we have shown that the high $v_{\rm los}$ features seen towards the bar in APOGEE are likely due to preferentially young stars on orbits moving along the major axis of the bar. They move close to the plane, which is why the feature disappears at high latitudes. The most important orbit family contributing to the feature are x_1 orbits, but a variety of more complex orbits also make significant contributions. Despite its simplicity, our model is the first shown to match the detailed kinematics in the bar region, and hence its late stages can serve as a blueprint for further and more detailed studies.

ACKNOWLEDGEMENTS

It is a pleasure to thank James Binney for helpful discussions and comments on the manuscript. We are grateful to Mattia Sormani and Evgeny Vasilyev for helpful comments. This work was supported by the UK Science and Technology Facilities Council through grant ST/K00106X/1 and by the European Research Council under the European Union's Seventh Framework Programme (FP7/2007-2013)/ERC grant agreement no. 321067. The simulations for this paper were performed on the Oxford Berg Cluster, a DiRAC Facility jointly funded by STFC, the Large Facilities Capital Fund of BIS, and the University of Oxford.

REFERENCES

Ahn C. P. et al., 2014, ApJS, 211, 17
Allende Prieto C. et al., 2008, Astron. Nachr., 329, 1018
Antoja T. et al., 2014, A&A, 563, A60
Aumer M., Binney J. J., 2009, MNRAS, 397, 1286
Babusiaux C. et al., 2014, A&A, 563, A15
Bedin R. L., Cassisi S., Piotto G., Castelli F., Salaris M., Momany Y., Pietrinferni A., 2005, MNRAS, 357, 1038
Bensby T. et al., 2013, A&A, 549, A147
Berentzen I., Shlosman I., Martinez-Valpuesta I., Heller C. H., 2007, ApJ, 666, 189
Berrier J. C., Sellwood J. A., 2015, ApJ, 799, 213
Binney J., Tremaine S., 2008, Galactic Dynamics, 2nd edn. Princeton Univ. Press, Princeton, NJ
Binney J., Gerhard O. E., Stark A. A., Bally J., Uchida K. I., 1991, MNRAS, 252, 210
Bland-Hawthorn J., Cohen M., 2003, ApJ, 582, 246
Blitz L., Spergel D. N., 1991, APJ, 379, 631
Bovy J., Rix H.-W., Liu C., Hogg D. W., Beers T. C., Lee Y. S., 2012, ApJ, 753, 148
Contopoulos G., Papayannopoulos T., 1980, A&A, 92, 33
Dame T. M. et al., 1987, ApJ, 322, 706
Debattista V. P., Sellwood J. A., 2000, ApJ, 543, 704
Debattista V. P., Ness M., Earp S. W. F., Cole D. R., 2015, preprint (arXiv:1507.01433)
Dehnen W., 2000, AJ, 119, 800
Dubinski J., Berentzen I., Shlosman I., 2009, ApJ, 697, 293
Eisenstein D. J. et al., 2011, AJ, 142, 72
Fraternali F, Binney J. J., 2008, MNRAS, 386, 935
Friedli D., Benz W., 1995, A&A, 301, 649
Hill V. et al., 2011, A&A, 534, A80
Li Z.-Y., Shen J., Rich R. M., Kunder A., Mao S., 2014, ApJ, 785, L17
Lynden-Bell D., 1979, MNRAS, 187, 101
Majewski S. R. et al., 2015, preprint (arXiv:1509.05420)
McMillan P. J., 2011, MNRAS, 414, 2446
Molloy M., Smith M. C., Evans N., Shen J., 2015, preprint (arXiv:1505.04245)
Nelson D., Vogelsberger M., Genel S., Sijacki D., Kereš D., Springel V., Hernquist L., 2013, MNRAS, 429, 3353
Nidever D. L. et al., 2012, ApJ, 755, L25
Patsis P. A., Athanassoula E., Quillen A. C., 1997, ApJ, 483, 731
Pietrinferni A., Cassisi S., Salaris M., Castelli F., 2004, ApJ, 612, 168
Pietrinferni A., Cassisi S., Salaris M., Percival S., Ferguson J. W., 2009, ApJ, 697, 275
Piffl T. et al., 2014, MNRAS, 445, 3133
Portail M., Wegg C., Gerhard O., Martinez-Valpuesta I., 2015a, MNRAS, 448, 713
Portail M., Wegg C., Gerhard O., 2015b, MNRAS, 450, L66
Roškar R., Debattista V. P., Quinn T. R., Wadsley J., 2012, MNRAS, 426, 2089
Schönrich R., 2012, MNRAS, 427, 274
Schönrich R., Binney J., 2009, MNRAS, 396, 203
Schönrich R., Aumer M., Sale S. E., 2015, preprint (arXiv:1507.02695)
Sellwood J. A., Carlberg R. G., 1984, ApJ, 282, 61
Sheth K., Vogel S. N., Regan M. W., Teuben P. J., Harris A. I., Thornley M. D., 2002, AJ, 124, 2581
Sormani M. C., Binney J., Magorrian J., 2015, preprint (arXiv:1507.03078)
Springel V., 2005, MNRAS, 364, 1105
Voglis N., Harsoula M., Contopoulos G., 2007, MNRAS, 381, 757
Wegg C., Gerhard O., 2013, MNRAS, 435, 1874
Wegg C., Gerhard O., Portail M., 2015, MNRAS, 450, 4050
Yurin D., Springel V., 2014, MNRAS, 444, 62
Zasowski G. et al., 2013, AJ, 146, 81
Zoccali M. et al., 2014, A&A, 562, A66

This paper has been typeset from a TEX/LATEX file prepared by the author.